J. Fluid Mech. (2010), *vol.* 660, *pp.* 55–86.
doi:10.1017/S0022112010002545

Synoptic velocity and pressure fields at the water–sediment interface of streambeds

M. DETERT[1]†, V. NIKORA[2] AND G. H. JIRKA[1]

[1]Institute for Hydromechanics, Karlsruhe Institute of Technology, Kaiserstrasse 12, D-76128 Karlsruhe, Germany

[2]School of Engineering, University of Aberdeen, Fraser Noble Building, Kings College, Aberdeen AB243UE, UK

(Received 17 April 2009; revised 19 April 2010; accepted 26 April 2010; first published online 16 August 2010)

This paper presents a comprehensive study of the near-bed hydrodynamics at non-moving streambeds based on laboratory experiments in open-channel flows. Pressure and velocity measurements were made with an array of up to 15 miniaturized piezo-resistive pressure sensors within the bed and slightly above it, and a two-dimensional particle-image-velocimetry (PIV) system measuring in streamwise vertical or horizontal planes. Three different types of bed materials were studied covering typical natural streambed conditions. The range of the global Reynolds number covered in the experiments was from 20 000 to 200 000. This study provides new insights into the flow structure over gravel beds based on the PIV measurements in both streamwise vertical and horizontal planes. In a streamwise vertical plane, large-scale wedge-like flow structures were observed where a zone of faster fluid over-rolled a zone with slower fluid. The resulting shear layer was inclined along the flow at an angle of 10°–25° to the bed, and was populated with clockwise rotating eddies. This mechanism occurred with sufficient frequency and shape to leave an 'imprint' in the velocity statistics. Typically, the described flow pattern is formed near the bed and is approximately scaled with the height of the logarithmic layer, although the biggest structures extended over the whole flow depth. In a horizontal near-bed plane, turbulent structures formed a patched 'chessboard' pattern with regions of lower and higher velocities that were elongated in the streamwise direction. Their lateral extension was typically two to four times the equivalent sand roughness with lengths up to several water depths. The dimensions of the regions were increasing linearly with the distance from the bed. These findings are consistent with conceptual models originally developed for smooth-wall flows. They also support observations made in rough-bed flume experiments, numerical simulations and natural rivers. Spatial fields of bed-pressure fluctuations were reconstructed by applying Taylor's frozen turbulence hypothesis on time data obtained with an array of pressure sensors. Based on the conditional sampling of velocity patterns associated with pressure-drop events a distinct bed-destabilizing flow-pressure pattern was identified. If a high-speed fluid in the wake of a large-scale wedge-like flow structure reaches the vicinity of the bed, a phenomenon akin to a Bernoulli effect leads to a distinctive low-pressure pattern. The resulting force may exceed the particles' submerged weight and is assumed to be able to give an initial lift to the particle. As a result, the exposed area of a

† Present address: VAW, ETH Zurich, Gloriastrasse 37/39, CH-8092 Zurich, Switzerland. Email address for correspondence: detert@vaw.baug.ethz.ch

particle is amplified and its angle of repose is reduced, increasing the probability for entrainment.

Key words: channel flow, pattern formation, vortex dynamics

1. Introduction

Kline *et al.* (1967) showed that turbulent flow is not simply chaotic, but includes well-organized coherent structures. Inspired by these findings, various studies of coherent structures have been carried out thereafter for flows over both smooth walls (e.g. Head & Bandyopadhyay 1981, Zhou, Adrian & Balachandar 1996 and Adrian, Meinhart & Tomkins 2000*b*) and rough walls (e.g. Grass, Stuart & Mansour-Tehrani 1991, Shvidchenko & Pender 2001, Stösser, Rodi & Fröhlich 2005, Hurther, Lemmin & Terray 2007 and Hardy *et al.* 2009). Macroturbulent coherent structures in natural aquatic systems appear to be similar to those reported for flows in laboratory experiments, also being elongated in shape and scaled with the flow depth (Roy *et al.* 2004). Sutherland (1967) and Jackson (1976) were among the first who highlighted relations between coherent structures and sediment erosion and transport in natural aquatic systems. As an example, subsequent experimental studies have shown that these structures play an important role at the incipient point of grain motion (e.g. Sumer & Oguz 1978, Sumer & Deigaard 1981, Drake *et al.* 1988, Sechet & Le Guennec 1999, Hofland & Booij 2004 and Cameron *et al.* 2006). Thereby, progress in sediment-transport studies may be directly dependent on the advancement of current understanding of coherent structures formed at the sediment bed–flow interface. The study reported in this paper follows this direction.

In his pioneering study, Sutherland (1967) proposed a sediment-entrainment hypothesis based on the concept of turbulent eddies breaking into the viscous sublayer and acting directly on the particles at the granular surface. Although the details of the process conceptualized by Sutherland are not totally correct in the light of present knowledge of turbulent structures, his hypothesis delineates the basic mechanics that was later observed by Drake *et al.* (1988) in a field experiment. Drake *et al.* filmed the bedload transport and observed sediment motions consistent with the effect of sweep-like downwards-moving high-speed fluid parcels impinging on the bed. Subsequent studies have shown that these events are probably most important in bedload transport at low average transport rates. As an example, Nelson *et al.* (1995) used synchronized laser Doppler velocimetry (LDV) and high-speed cinematography to show that sweeps and outward interactions together are much more effective in moving sediments compared to ejections and inward interactions. This finding is in agreement with a recent laboratory study with extensive use of particle-image-velocimetry (PIV) techniques reported in Cameron *et al.* (2006). Further support to this finding is provided by Wu & Jiang (2007), who numerically investigated the effect of bursting events on sediment entrainment. Their results show that the entrainment of fine sediment mixtures is dominated by the lifting mode, whereas the entrainment of coarse sediments is dominated by rolling. Sweeps are consistently found to be the most significant contributor to entrainment under various types of sediment mixtures. However, Nino & García (1996) and Sechet & Le Guennec (1999) provide solid evidence that ejections may be as important events for sediment motion as sweeps, if not more important.

A new light on this issue has been recently shed by Hofland & Booij (2004), who measured the flow fields during the actual entrainment of a single stone using a two-dimensional PIV technique. In order to determine the flow structures that are responsible for the particle entrainment the flow field was conditionally averaged over many entrainment events. The resulting flow patterns show that two structure types are most probably responsible for the entrainment. The first structure type is presented by small-scale structures embedded into a much larger sweep event representing the second type. The entrainment begins with an impact of a small-scale structure that initiates the motion of the stone, and then a large-scale sweep moves the stone further over its pivot point.

Most of the previous experimental studies have been based on point-velocity measurements (e.g. LDV) or on a vertical-plane PIV. These studies have mainly focused on flows over impermeable beds while the more realistic case of permeable beds has not been studied systematically due to technical limitations. However, with recent advances in measurement instrumentation it has become possible to address this issue by combining high-resolution acoustic and PIV techniques for velocity measurements with miniature pressure measurements (e.g. Hofland, Booij & Battjes 2005). The goal of the present study is to follow this route and extend the synoptic measurements from a single-grain view to a larger multi-grain scale, which should provide a more comprehensive identification and description of flow structures at the sediment–flow interface. As a first step, in this paper we focus on the stable granular beds with no particle entrainment. The main targets include identification of (i) flow patterns from vertical-plane and horizontal-plane PIVs, (ii) bed-pressure-fluctuation patterns and (iii) correlations of flow patterns with pressure-fluctuation patterns potentially significant for particle entrainment.

2. Experimental set-up

2.1. *Laboratory facilities*

The experiments were carried out in a rectangular laboratory flume at the Institute for Hydromechanics (IfH), Karlsruhe Institute of Technology, with a working part length of 17.0 m and a width of $B = 0.9$ m. The water depth ranged from $h = 0.13$ to 0.22 m. A right-handed coordinate system is implied, where x is directed along the flow, y is upwards vertical and z is in the transverse direction. Further, $x = 0$ holds at the middle point of the measurement area, $y = 0$ is defined as the origin of the log velocity distribution obtained from the analysis of the measured $\langle\overline{u}\rangle(y)$ using a best-fit technique (here an overbar defines time averaging and angle brackets define spatial averaging in a plane parallel to the mean bed) and $z = 0$ is on the centreline of the flume. The velocity components u, v and w correspond to x, y and z, respectively. The flume inlet was at $x = -10.5$ m to guarantee a fully developed open-channel flow at the measurement area. The flume outlet at $x = +6.5$ m was controlled by vertical thin-plate vanes. Hence, influences on flow conditions at the measurement site of both inlet and outlet can be neglected. The bottom of the flume had a slope of $S_b = 0.5\,‰$. The experiments were made with three different bed particles: spheres, uniform gravel and gravel from the river Rhine, which formed 0.10 m thick sediment layers. The slopes of the sediment bed surfaces were made equal to the flume slope. However, due to a slight inevitable erosion that occurred at the outlet, the bed surface slope slightly increased over the last 3 m of the flume. The water depth h was measured at three points at $x = [-9.33, 0.00, +4.42]$ m by ultrasonic probes. They were mounted on external cylindrical water tanks that were in hydraulic interconnection with the

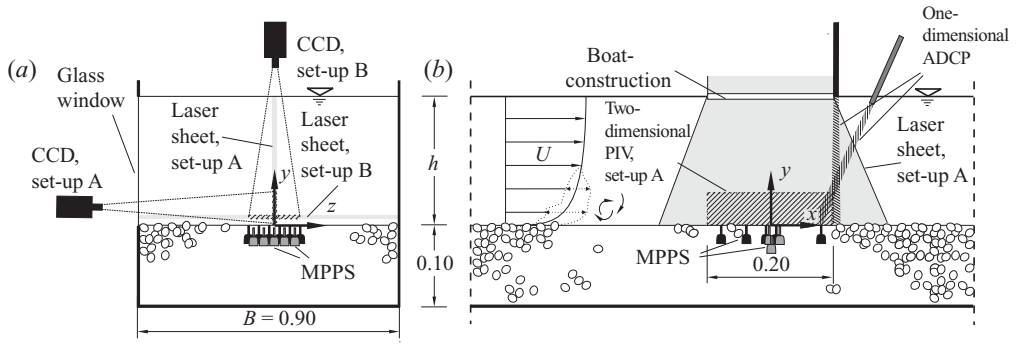

FIGURE 1. Sketch of the experimental set-up. Dimensions in metres, not to scale. (*a*) View in the streamwise direction, with both two-dimensional PIV arrangements of set-ups A and B. (*b*) Side view, where the positions of the one-dimensional ADCP probe can also be seen.

porous bed via flexible tubes (25 mm in diameter). With this set-up, fluctuations and small-scale oscillations of the actual water level were low-pass-filtered.

Figure 1 illustrates the set-up of the measurement instruments used in the experiments. It consisted of an array of up to 15 miniature piezo-resistive pressure sensors (MPPS) located within and slightly above the sediment layer, and a two-dimensional PIV system. The latter technique was used for measuring velocities both in a centreline vertical plane perpendicular to the bed (xy-plane: set-up A), and in horizontal planes at $y_t = [5, 15]$ mm as well as at $y_t = [5, 9, 23]$ mm above the upper gravel grain crest and the sphere crest, respectively (xz-plane: set-up B). Optical access to the measurement site was available through a 4.0 m long glass window on the left flume wall. Additional information on velocity fields was gained with an acoustic Doppler current profiler (ADCP, Signal Processing, Lausanne, Switzerland) in order to supplement and cross-check the PIV results, as well as to provide information on flow properties within the outer layer, which was not covered by PIV measurements. Typically, a single data-acquisition episode was carried out for 205 s using, simultaneously, 15 MPPS, the two-dimensional PIV system and an ADCP probe. The following sections provide more details on the measurement systems.

2.2. *Particle image velocimetry*

A commercial two-dimensional PIV LaVision system was used. This PIV package includes camera, laser illumination, frame grabber, controlling and evaluation software. Digital images could be recorded with a 1280×1024 pixel^2 12 bit camera with a charge-coupled device (CCD) sensor (Flowmaster 3S). To get a satisfying spatio-temporal resolution, a double-frame mode had to be used. In this mode, two images are captured within a very short time. The first image is not read out directly (as in a simple single-frame mode), but shifted to the storage position on the camera chip and then the second frame is taken. For the experiments, an interval time of 2–8 ms was used to acquire one double frame, to optimize accuracy.

For PIV measurements, the flow was seeded with nearly neutrally buoyant tracer particles (Vestosint® polyamide powder, type 1101, $d \simeq 80$–$200\,\mu$m, $\rho = 1.06$ kg m^{-3}). The flow field was illuminated with a dual-cavity Q-switched Nd:Yag laser with a pulse energy of up to 25 mJ per pulse. The emitted light was green at a wavelength of 532 nm. The laser sheet was enlarged by a top-hat lens and had a thickness of 1–2 mm. For set-up A, the laser sheet was guided into the water through a glass bottom of a streamlined hull structure that was 15 mm wide and 300 mm long. With

this set-up, potential disturbing effects of the free surface on the laser sheet were avoided. Typically, the hull was immersed by <5 mm and caused small surface waves in the wake, without affecting the flow in the near-bed region. This illumination was applied for a vertical plane at the centreline of the flume; no measurements were made with the sheet laterally translated from the centreline. For velocity measurements in a horizontal plane (set-up B), a similar structure for the camera was used to avoid disturbing reflections from the water surface. The streamlined boat-shaped structure was 100 mm wide and 300 mm long. As a supplement for set-up B, a wide-angle lens (Nikon F-mount, 14 mm, distortion <1 %) was used to increase the observed flow area. This lens provided high resolution combined with high luminosity, which is important for maximizing the measurement accuracy.

At set-up A, the size of the camera frames was reduced in a vertical direction to $1280 \times 384\,\text{pixel}^2$ to increase the read-out duration of the camera chip. Thus, a constant double frame rate of $f = 8.5\,\text{Hz}$ was achieved, leading to 1740 double frames within 205 s, well exceeding recommendations for a measurement duration in fluvial boundary layers (Buffin-Bélanger & Roy 2005). The camera was adjusted to a streamwise vertical xy-plane of $202.0 \times 60.5\,\text{mm}^2$ directly above the bed, so that the observation of the outer flow was not possible. At set-up B, the size of the camera frames was laterally shortened to $1280 \times 800\,\text{pixel}^2$ for the experiments with the uniform gravel and the Rhine gravel. For the experiments with spheres, the full frame size was read out. Consequently, double frame rates of $f = 4.9\ (4.0)\,\text{Hz}$ for the experiments with the gravel (spheres) were achieved, leading to 1003 (819) double frames within 205 s. Typically, a horizontal measurement window of $160 \times 100\,\text{mm}^2$ ($144 \times 115\,\text{mm}^2$) was used.

The image processing was done by a multi-pass cross-correlation method with a discrete window offset, where the intermediate vector fields were smoothed by a $3 \times 3\,\text{pixel}^2$ Gaussian filter. A final interrogation window size of $16 \times 16\,\text{pixel}^2$ with 50 % overlap was chosen. Thus, the vector spacing was half the spatial resolution in each case. The latter resulted in 2.52 mm for set-up A; for set-up B it was 1.98–2.06 mm (gravel) and 1.56–1.90 mm (spheres), depending on the distance between the camera lens and the horizontal PIV slice. The resulting vectors were checked using a median filter, an absolute allowed vector range, and the distinctiveness of the highest correlation peak. Typically, 75 %–95 % of all vectors within one double frame were validated, depending on the density and homogeneity of the seeding material. Using spectral analysis we found that the vector fields obtained by the PIV system captured at least more than 95 % of the turbulence intensity (for details, see Detert 2008, pp. 64–66).

2.3. *Miniature piezo-resistive pressure sensors*

The main components for the MPPS were obtained from Aktiv Sensor GmbH, Berlin. The sensing elements ATD 0.040-G00-BG-K1408 and AU blank PGA-V0-D18A were assembled at the Institute for Hydromechanics to make their packaging most suitable for this study. Figure 2(*a*) gives a sketch of a pressure pick-up. Depending on the configuration, the pressure sensors may measure both the surrounding pressure and the velocity head. Thus, the sensed pressure provides a force per pinhole area in the direction of the pressure tube.

To miniaturize the pick-ups of the pressure transducers the amplifying blankets had to be arranged in an external box. The length of the flexible cables from the measurement site to the external amplifying board could not be shorter than 2.5 m, due to the limitations of the experimental facilities. Thus, the possibility of a slight

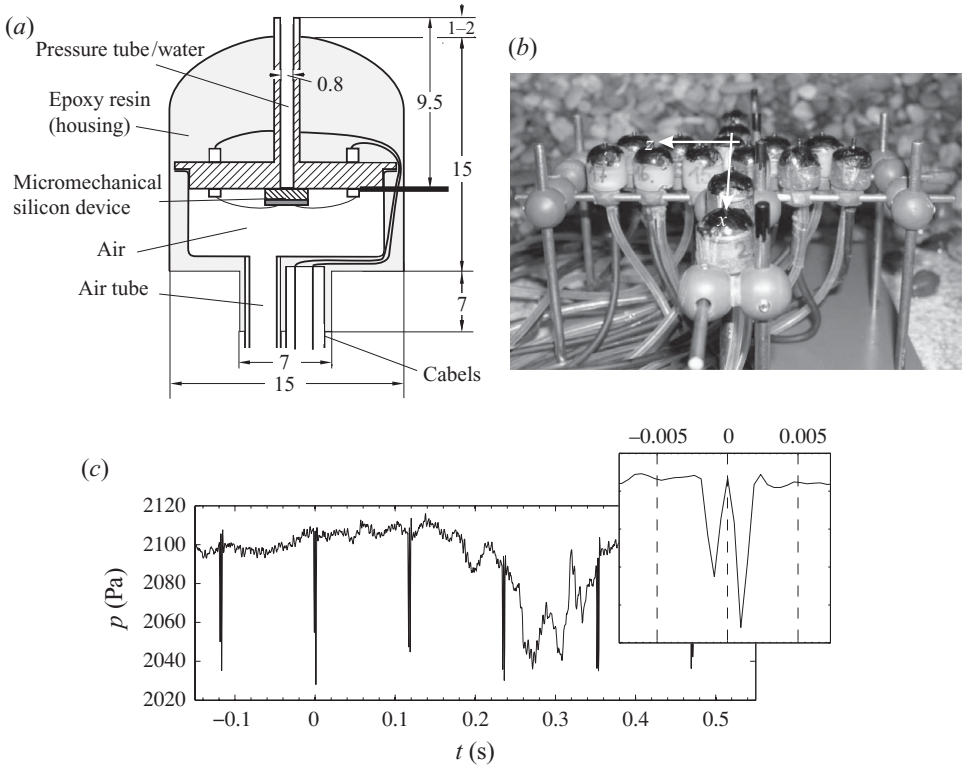

FIGURE 2. (*a*) Sketch of a pressure pickup (in millimetres). (*b*) Array of MPPS mounted on a grid, not covered by gravel yet. This arrangement was used in synchronous measurements of MPPS, PIV and ADCP. (*c*) Measurement to test the response time of the MPPS, where the sensor reacts on the double pulse of the PIV laser sheet of $\Delta t = 2$ ms.

'antenna effect' on pressure records had to be accepted. Flexible PVC tubes, 2.5 m long, were used to provide atmospheric pressure within the pick-ups. The MPPS pick-ups were encapsulated with a slowly hardening epoxy resin and sealed up with clear varnish to make them water-resistant. A fully assembled pressure pick-up was shaped to locally replace a single gravel element with a diameter of 15 mm. In this, the set-up guaranteed an almost non-perturbed roughness layer. The so-built sensors were two-point-calibrated by Aktiv Sensor GmbH to [1, 9] V for [0, 4] kPa by an accuracy of less than 1.0 % of full scale. The response time guaranteed by the manufacturer is <10 ms, and is determined by signal conditioning and the amplifying blankets performance. To avoid aliasing effects due to high-frequency noise (>2 kHz), the data records were made at $f \simeq 2125.7$ Hz, with follow-up smoothing by a fourth-order Butterworth low-pass filter with a cut-off frequency of 500 Hz (Data Translation SAK 52-150-501-10). A 16-bit analog-to-digital converter (ADC; Data Translation 321) allowed a pressure resolution at approximately 0.15 Pa. For deployment in the flume, the sensors were fixed on a grid. Figure 2(*b*) gives an example of an array of 15 MPPS, arranged to identify the bed area where lift forces are applied.

Synchronous measurements with all instruments involved were started by a TTL (transistor–transistor logic) trigger pulse from the PIV system. The TTL signals of the PIV frame grabber were additionally recorded via the 16-bit ADC, to enable a fine-tuning of the synchronization afterwards. Furthermore, tests in the flume showed

Run no.	Bed	$[d_{15}, d, d_{85}]$ (mm)	ϕ	k_f (m s^{-1})	ρ_s (10^3 kg m^{-3})	Packing
sph1	Spheres	[25.4]	0.26	1.6	1.36	Densest
uni6, uni9	Uniform gravel	[7.7, 10.2, 13.2]	0.39 ± 0.02	0.7	2.46	Loose
rhi9	Rhine, armoured	[13.8, 26.1, 38.8]	0.33 ± 0.02	1.5	2.51	Loose

TABLE 1. Parameters of the bed materials: spheres, uniform gravel and gravel from the river Rhine (armouring layer).

that the MPPS were able to react within 2 ms. In one measurement arrangement four sensors were aligned within the laser sheet. The laser double pulses were clearly identifiable in the signal, as shown in Figure 2(*c*). This unforeseen effect was used to validate the synchronization of the PIV and the MPPS.

2.4. *Bed material*

Flow measurements were performed over three different types of porous beds: uniform gravel, gravel from the river Rhine and spheres. Table 1 summarizes the properties of the bed materials. The grain sizes d_i were gained by sieve analysis. The weighted mean of the whole grain size distribution is represented by d, following Meyer-Peter & Müller (1949). It was observed that for uni $d \approx d_{50}$ and for rhi $d \approx d_{70}$. The permeability coefficient k_f was obtained from Hazen's (1892) equation for the uniform gravel and the Rhine gravel, and from Kozeny–Carman's equation (Carman 1956) for the spheres. The sediment porosity is assessed as $\phi = V_f / V_o$ ($1 \geqslant \phi \geqslant 0$), where V_f is the volume of the fluid within the total volume V_o. The porosity was determined by a volumetric method in an external tank. The density of the stone is denoted by ρ_s.

Gravel with a fairly narrow size distribution was used as a basic bed material (uni6 and uni9) in our study. This material occupies an intermediate position between more variable gravel particles found in natural streams and single-size spheres, often used in mathematical models and numerical simulations. In addition, experiments were also conducted with the gravel material collected from the river Rhine (rhi9). Working with this natural gravel, we attempted to preserve the porous bed texture and consequently the observed rough-bed flow was as natural as it was possible within a laboratory experimental set-up. The Rhine material was collected at low-flow conditions (2 August 2006) from a gravel bank ~10 km downstream of the Iffezheim barrage. The armouring layer and the bimodal subsurface layer ($[d_{10}, d_{60}] = [0.4, 14.7]$ mm) were sampled and removed separately. To simulate the Rhine bed effects in the experiments, the uniform gravel in the flume was replaced with the Rhine material in a 4.5 m long ($x = -4.0$ to $+0.5$ m) section covering the whole flume width. The third bed structure installation explored in this study was a three-particle layer of spheres in the densest packing (sph1). This bed type provided a simplified bed geometry, as often used nowadays in numerical and analytical models. The spheres were originally manufactured as balls for deodorant roll-ons but for the experiments they were filled with fine sand to secure their stability on the bed. In contrast to the Rhine material placement, the uniform gravel bed was only partly replaced by spheres. Three layers of spheres were inserted at $x = -460$ to $+290$ mm and $z = -150$ to $+150$ mm. The uppermost layer was lengthened upstream to $x = -1160$ mm to provide fully developed sphere-flow conditions. The porosity $\phi = 0.26$ for spheres in pyramidal packing was taken from an analytical–numerical derivation of Bowen & Radin (2003).

Run no.	$Q\,(\mathrm{s}^{-1})$	$U\,(\mathrm{m\,s}^{-1})$	$u_*\,(\mathrm{m\,s}^{-1})$	$Re_h\,(\times10^3)$	$Re_{*h}\,(\times10^3)$	$Re_{*\delta}\,(\times10^3)$	Re_{*d}	Fr_h	$Fr^2_{*\Delta}\equiv\Theta$
sph1	18.6	0.160	0.015	20.6	1.94	1.88	377	0.14	0.003
uni6	120.0	0.667	0.063	133.4	12.60	11.03	643	0.46	0.027
uni9	180.0	0.948	0.095	200.0	20.05	14.73	969	0.68	**0.062**
rhi9	180.0	0.930	0.086	200.0	18.49	13.33	2245	0.64	0.019

TABLE 2. Flow properties. Q: flow rate; $U=Q/(Bh)$: bulk velocity; u_*: shear velocity. Reynolds numbers: $Re_h=Uh/\nu$; $Re_{*h}=u_*h/\nu$; $Re_{*\delta}=u_*\delta_h/\nu$; $Re_{*d}=u_*d/\nu$. Froude numbers: $Fr_h=U/\sqrt{gh}$, with g being the gravitational acceleration; $Fr^2_{*\Delta}=u_*^2/(\Delta gd)$, where $\Delta=\rho_s/\rho-1$, with ρ being the density of water.

Run no.	h (mm)	δ_h (mm)	k_s (mm)	δ_{yo} (mm)	$y(\langle\overline{u'v'}\rangle_{max})$ (mm)	η (mm)
sph1	129	125	20.5 ± 1.5	5.0 ± 0.5	13	0.44
uni6	200	175	26.5 ± 3	2.6 ± 2	12	0.17
uni9	211	155	26.5 ± 3	2.6 ± 2	12	0.12
rhi9	215	155	15.5 ± 3	6.6 ± 3	13	0.14

TABLE 3. Geometric parameters. h: water depth measured by ultrasonic probes; $\delta_h=y(\overline{u}_{max})$; d: characteristic grain size; k_s: equivalent sand roughness; δ_{yo}: zero-plane displacement; η: Kolmogorov length scale.

3. Background conditions and bulk parameters

3.1. *Flow properties*

Table 2 summarizes the experimental conditions for each run used in this study. All runs relate to stable beds although it should be noted that conditions for uni9 are near-critical (Shields' parameter Θ is 0.062, highlighted in bold) and thus very occasional particle movements were observed, as one would expect (e.g. Buffington & Montgomery 1997). The bed was not water-worked for the experimental runs to avoid damaging the MPPS and to keep the height of the bed level adjusted to the calibrated measurement set-up. The flow conditions for the Rhine bed (rhi9) were adopted from uni9, keeping Re_h the same. The experiments with the bed formed by spheres were conducted at lower Re_h numbers to keep them in the range that can nowadays be achieved in numerical simulations. The integers [1, 6, 9] at the end of the run identificators refer to the approximate ratios of Q_i, U_i and $Re_{h,i}$ to those of sph1. The bulk Froude number Fr_h is well below 1.0 for all runs, reflecting sub-critical-flow conditions. The squared densimetric Froude number $Fr^2_{*\Delta}$, also known as the Shields parameter Θ, varies from 0.003 to 0.062, in agreement with the visually observed particle stability on the bed.

Table 3 presents the relevant geometric parameters. The targeted water depth was $h=200$ mm. However, preliminary tests showed that this depth was difficult to achieve at the measurement site for uni9 and rhi9. The convex water surface due to non-uniform flow conditions led to a minimum of 211 and 215 mm, respectively. For sph1, a lower water depth was chosen to obtain flow conditions with lower Reynolds number. The depth was decreased to $h=129$ mm, i.e.the minimum possible depth compatible with the geometrical boundaries of the measurement set-up.

The centreline value of the dip distance from the bed $\delta_h=y(\overline{u}_{max})$ was determined from $\overline{u}(y)$ gained by the ADCP that provided a spatial resolution of 5 mm. Except

Index	$\langle\tau_o\rangle_{us}$ (N m^{-2})	$\langle\tau_o\rangle_{ds}$ (N m^{-2})	$\langle u_*\rangle_{us}$ (m s^{-1})	$\langle u_*\rangle_{ds}$ (m s^{-1})	u_{*uv} (m s^{-1})	$u_{*log} \equiv u_*$ (m s^{-1})	τ_o (N m^{-2})
sph1	0.27	0.16	0.016	0.013	0.013	0.015	0.23
uni6	3.45	3.70	0.059	0.061	0.059	0.063	3.97
uni9	8.40	20.5	0.092	0.143	0.087	0.095	9.03
rhi9	12.5	12.5	0.112	0.112	0.081	0.086	7.40

TABLE 4. Shear parameters. $\langle\tau_o\rangle$ is calculated by (3.1), and $\langle u_*\rangle$ was derived from them by applying (3.2). u_{*uv} was estimated by extrapolating $-\langle\overline{u'v'}\rangle$ to the mean bed level. $u_* \equiv u_{*log}$ is gained from log-law fit.

for sph1, the presence of the dip phenomenon is evident for all runs, as $\delta_h/h < 1.0$ holds. For the uniform flow conditions of uni6 the dip phenomenon is the weakest ($\delta_h/h \simeq 0.88$), whereas the centreline $\overline{u}_{max}$ for the experiments with the accelerated flows was found at approximately $h/4$ below the water surface, consistent with other studies of accelerated open-channel flows (e.g. Song & Graf 1994). The equivalent sand roughness k_s was obtained by fitting the centreline velocity profile $\overline{u}(y)$ to the log-law $\langle\overline{u}\rangle(y)/u_* = 2.44\ln(y/k_s) + (8.5 \pm 0.2)$, which was clearly observed within the near-bed layer up to 20 %–25 % of the flow depth. The value of $k_s/d = 2.6$ for uni6 and uni9 is in the typical range of $k_s/d = 1$–4, as can be found for natural beds. However, the ratio $k_s/d = 0.6$ for the Rhine bed (rhi9) resembling a natural armoured layer appears to be smaller than expected. The reason for this is unclear. One possible explanation is that the use of d as a denominator may be misleading here as particle shape and orientation on the bed were not taken into account. For the experiments with spheres $k_s/d = 0.8$ holds, similar to the range of $k_s/d = 0.68$–0.82 in Grass *et al.* (1991) and $k_s/d = 0.67$ in Defina (1996). The estimates of the zero-plane displacement δ_{yo} for the log-law, defined as the distance between the roughness tops, $y_t = 0$, and the origin for the logarithmic layer, $y = 0$, and obtained using the same best-fit technique as for k_s, are shown in table 3. The values of δ_{yo} found for the uniform gravel and the Rhine gravel are in general agreement with the available estimates of other researchers, i.e.$\delta_{yo} = 0.25\,d$ (e.g. van Rijn 1984), although it could not be determined more accurately than $\pm$(2–3) mm. For the experiments with spheres, $\delta_{yo} = 0.20\,d$ holds. This value is similar to that reported by Grass *et al.* (1991), who found (0.20–0.22) d from laboratory experiments, and to 0.22 d reported by Stösser *et al.* (2005) from large eddy simulation (LES) studies. Another useful measure characterizing the potential effects of the bed roughness and secondary currents as well is the distance $y(\langle\overline{u'v'}\rangle_{max})$ that follows from the PIV data. This distance reaches 10 %–15 % of the water depth, slightly increasing with decreasing Reynolds numbers. The smallest flow scale, the Kolmogorov microscale η, could not be directly measured and therefore was estimated approximately, following Nezu & Nakagawa (1993, p. 30). The obtained values are in the range of $\eta = 0.12$–0.44 mm.

3.2. *Bed shear stress*

The estimates of the bed shear stress τ_o and the shear velocity u_* are given in table 4. The subscripts $\langle\cdots\rangle_{us}$ and $\langle\cdots\rangle_{ds}$ denote the spatial averages of the upstream area ($x = -9.33$ to 0.0 m) and the downstream area ($x = 0.0$ to $+4.42$ m), respectively. The spatially averaged $\langle\tau_o\rangle$ and $\langle u_*\rangle$ are derived from an integral momentum equation for

a non-uniform open-channel flow by applying

$$\tau_o(x) = \rho g S_b R_h - \rho \left(g R_h + \beta U^2 \frac{R_h}{h} \right) \frac{\mathrm{d}h}{\mathrm{d}x}, \tag{3.1}$$

and

$$u_* = \sqrt{\tau_o/\rho}. \tag{3.2}$$

In (3.1), R_h is the hydraulic radius, and the momentum non-uniformity parameter $\beta = 1.03$ is determined from both PIV and ADCP data. The bed slope S_b is constant and equal to 0.5 ‰. A comparison of the estimates obtained using (3.1) suggests that flow conditions for uni6 were very close to uniform (as for uni6, $\langle \tau_o \rangle_{us} \simeq \langle \tau_o \rangle_{ds}$ holds). However, the degree of uniformity for other runs was not as high: uni9 should be qualified as a slightly accelerated flow. For rhi9, the ultrasonic probe for $h\,(x = 0)$ showed unrealistic values and therefore the estimates were obtained for the whole flow length without subdivision into upstream and downstream parts. As the flow conditions for rhi9 are similar to those for uni9, the flow was also, most probably, slightly accelerating. The shear stress estimates for sph1 in table 4 suggest that flow conditions were reasonably close to uniform, similar to those for uni6. The obtained estimates are consistent with the empirical rule for open channels and natural rivers that $u_* = (0.05\text{–}0.10)\,U$.

The above bulk estimates of the bed shear stress and shear velocity were supplemented with estimates using two additional approaches: (i) u_{*uv} was estimated from the PIV measurements by extrapolating the centreline Reynolds stresses $-\rho\langle\overline{u'v'}\rangle$ to the mean bed level (Nikora *et al.* 2001); (ii) u_{*log} was gained by least-square fits of the mean centreline velocity $\overline{u}(y)$ to the log-law (same procedure as for k_s). The values of u_{*log} were obtained from independent PIV and ADCP measurements within a scatter of ± 3 %. The differences between u_{*uv} and u_{*log} are reasonably small, with values of u_{*log} being slightly larger than u_{*uv}, i.e. u_{*uv}/u_{*log} is about 90 ± 3 %, leading to differences in τ_o ($\propto u_*^2$) up to 13 %–17 %. This systematic difference most likely relates to the effects of flow non-uniformity and secondary currents (e.g. Nezu & Nakagawa 1993, p. 109), and therefore, in our further considerations we use u_{*log} as it is presumably less affected by these features, i.e.

$$\rho u_{*log}^2 \equiv \rho u_*^2 \equiv \tau_o. \tag{3.3}$$

Complete details on bulk turbulence statistics and their spatial distribution can be found in Detert (2008).

4. Flow structures

4.1. *Streamwise vertical view*

It is useful to start with a qualitative picture of large structures that can be seen on PIV images. Figure 3 shows a sequence of two consecutive instantaneous velocity fields, measured in a streamwise vertical plane over a spherical bed (sph1). A passage of two fluid regions can be observed, where a faster region represents a sweep event (Q_4, $u' > 0$, $v' < 0$) coupled with a slower fluid region that can be interpreted as an ejection event (Q_2, $u' < 0$, $v' > 0$). The shear layer between these regions is inclined along the streamwise direction under the angle of approximately 20°. Due to its higher propagation velocity, the faster flowing region over-rolls the slower near-bed region. The inclined shear layer separating these two regions is filled with small eddies, as suggested by the swirling strength λ_{ci}. This parameter is defined as the imaginary part

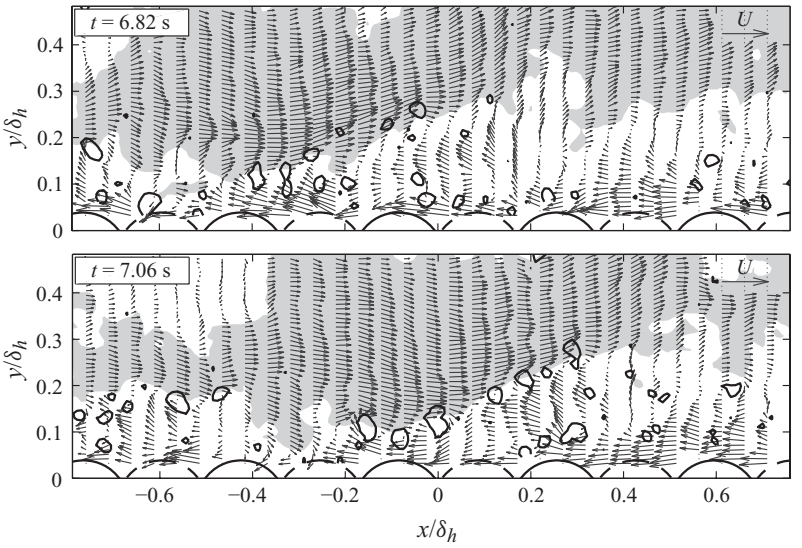

FIGURE 3. Sequence of instantaneous velocity fields for sph1, where the passage of a large-scale wedge-like fluid structure can be observed. The velocity field was filtered by a 2×2 filter. For visualization, the vectors are presented with a constant convection velocity $\boldsymbol{u}_c = [0.85U, 0]$ removed. In x, only every fifth vector is plotted. Contours of λ_{ci} highlight the location of vortex cores. The shading indicates that $\sqrt{(u^2 + v^2)} > U$. The shear layer between the faster and the slower moving fluid zones is densely populated with eddies.

of the complex eigenvalue of the velocity gradient tensor (e.g. Adrian, Christensen & Liu 2000*a*). For two-dimensional flow fields it can be expressed as

$$\lambda_{ci} = \max\left[0, -\frac{\partial u}{\partial y}\frac{\partial v}{\partial x} + \frac{1}{2}\frac{\partial u}{\partial x}\frac{\partial v}{\partial y} - \frac{1}{4}\left(\frac{\partial u}{\partial x}\right)^2 - \frac{1}{4}\left(\frac{\partial v}{\partial y}\right)^2\right]. \tag{4.1}$$

The qualitative picture of figure 3 agrees well with the physical model proposed by Adrian *et al.* (2000*b*) for the organization of vortex structures of the logarithmic layer in smooth-wall flows. In terms of Adrian *et al.* (2000*b*), the eddy cores in the shear layer of figure 3 represent hairpin vortex heads grouped into packages. (These structures are known as hairpin vortex packages (HVP).)

As can be seen in figure 4, the flow pattern described for sph1 is typical for all studied beds. Among these, the flow picture over the spheres-formed bed is most clear with easily identifiable vortex heads within the nearly straight shear layer. For the gravel bed experiments uni6, and rhi9, the wedge-like structures look less pronounced, although well recognizable as well. The inclination angles of the shear layer, 10°–25°, cover the same ranges as observed by Tomkins (2001) for air flows over hemispheres-covered wall in wind tunnels, and by Roy *et al.* (2004) in natural gravel bed rivers. The described wedge-like structures occur with a frequency of 0.2–2 Hz. Some of them are well defined, but to identify others some imagination is required. Occasionally, these structures are superimposed or interrupted with other structural features like large-scale rollers or declining ramps.

The next useful step in characterizing large-scale flow structures involves conditional averaging that may help in highlighting their specific features, as was suggested in Christensen & Adrian (2001) for smooth-bed flows. These authors introduced two-point correlations between the swirling strength and velocities as an objective

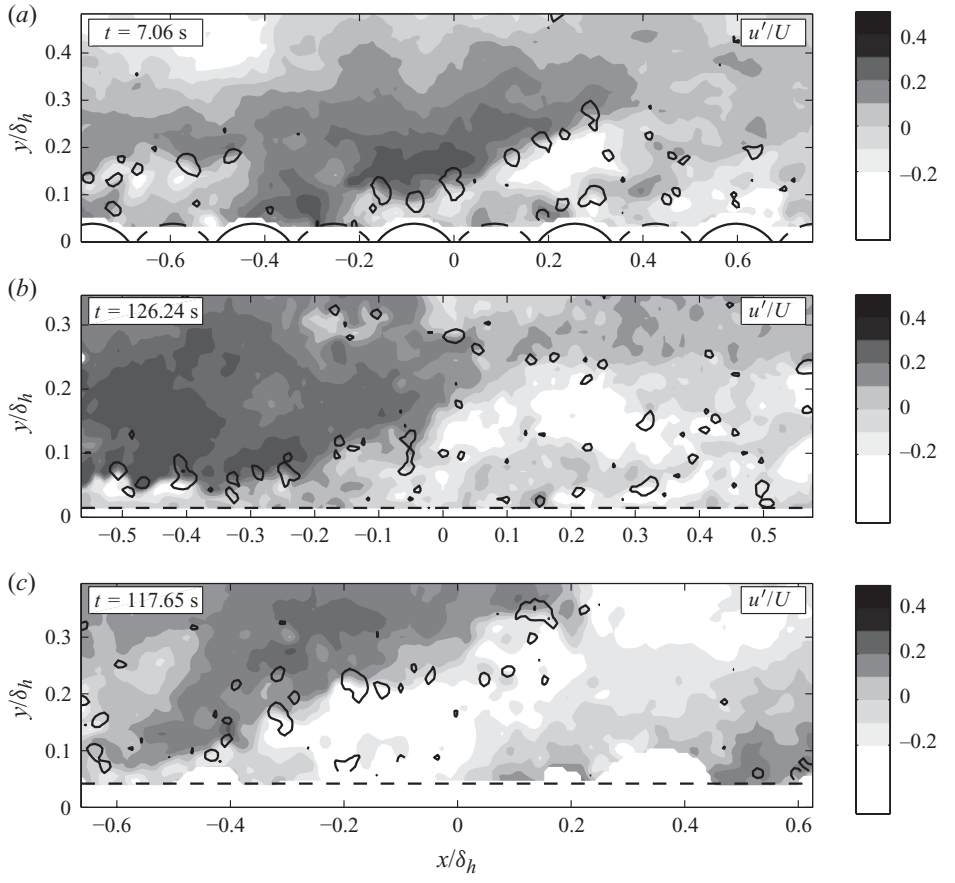

FIGURE 4. Typical pictures of wedge-like flow structures as observed for the flow over (*a*) spheres (sph1), (*b*) uniform gravel (uni6) and (*c*) Rhine gravel (rhi9). The velocity field was filtered by a 2×2 spatial filter. Contours of λ_{ci} are shown to highlight the location of vortex cores. The shading indicates u'/U in steps of 0.1.

measure of the conditionally averaged velocity field associated with the vortex heads. Here we apply essentially the same procedure to obtain estimates of similar correlation functions for rough-bed flows. A cross-correlation function $C_{\lambda u}(r_x, y)$ is defined as

$$C_{\lambda u}(r_x, y) = \frac{\langle \lambda_{ci}(x, y_{ref})\, u'(x + r_x, y) \rangle}{\sigma_\lambda(y_{ref})\, \sigma_u(y)}, \tag{4.2}$$

where r_x denotes the horizontal shift in x and y_{ref} is the reference height at which the swirling strength is taken. Note that $\lambda_{ci} \geqslant 0$ holds by definition; so $C_{\lambda u}(r_x, y)$ retains the sign of u'. Therefore, the correlation function includes some structural information on the flow organization within the vortex cores. The correlation function (see (4.2)) is normalized on the standard deviations of constituents.

Figure 5 illustrates the time-averaged correlation $\overline{C_{\lambda u}}$ for the experiments sph1, uni6 and rhi9. The correlation estimates are based on averaging 1740 'instantaneous' correlations corresponding to the frames of the velocity fields recorded within 205 s, thus minimizing statistical and sampling errors. The reference height, $y_{ref}/\delta_h \simeq 0.2$, was chosen to represent near-bed vortices, which are most relevant to the problem at hand.

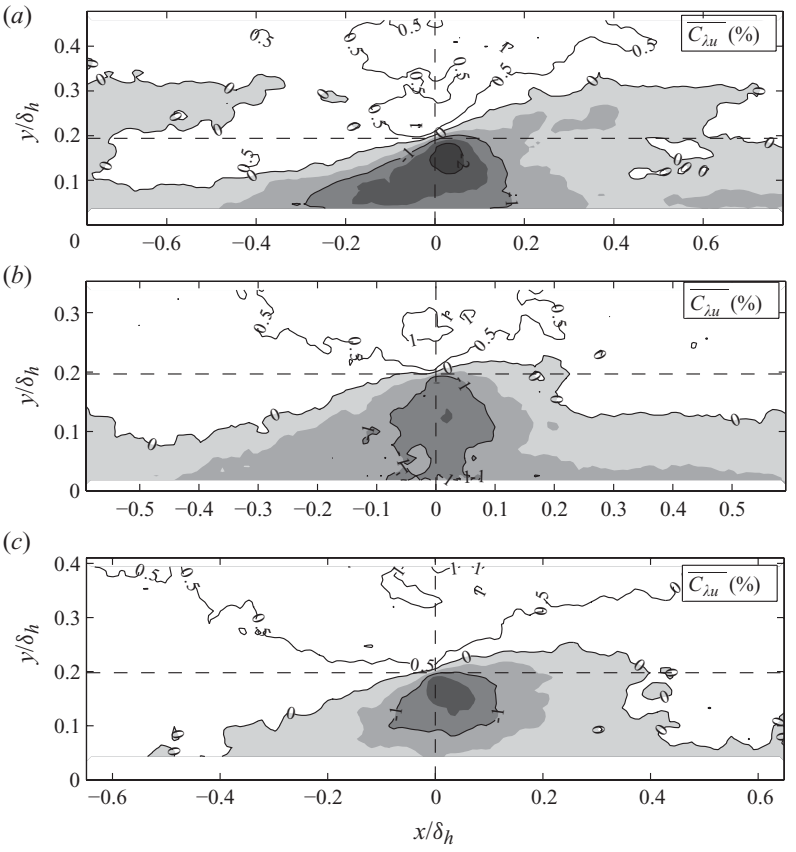

FIGURE 5. Time-averaged cross correlation $\overline{C_{\lambda u}}$ based on 1740 velocity fields of $u'(x, y)$ and $\lambda_{ci}(y_{ref}/\delta_h \simeq 0.2)$ for the structure over (*a*) spheres (sph1), (*b*) uniform gravel (uni6) and (*c*) Rhine gravel (rhi9). Spacing contours are in steps of 0.5 %. The result gives some evidence that mean wedge-like flow structures exist above rough walls, where a series of clockwise rotating eddies are located along a line inclined at approximately 10°–20° from the wall (see zero line).

The 'topography' of the correlation function for all three bed types is similar. A key feature of this topography is a narrow large-scale interface region separating domains of positive and negative values of $\overline{C_{\lambda u}}$. This region is inclined at approximately 10°–20°. The correlation function is negative below this interface region and positive above it. The positive domain of $\overline{C_{\lambda u}}$ above the interface region represents a faster flowing fluid compared to slow fluid motion within a negative domain below it. These features are consistent with the presence of clockwise-rotating vortex heads which are likely grouped along a line inclined at 10°–20°. The topography of $\overline{C_{\lambda u}}$ suggests that the instantaneous structures occur with sufficient frequency, strength and order to leave an 'imprint' on the flow statistics. These findings are similar to those of Christensen & Adrian (2001) for hydraulically smooth walls and and thus point out to the potential existence of the HVP or at least their signatures in rough-bed open-channel flows as well. The topographies of $\overline{C_{\lambda u}}$ for the experiments sph1, uni6 and rhi9 are very similar, indicating that the organization of large-scale wedge-like structures is relatively insensitive to roughness type, water depth and Reynolds number. Figure 5 also suggests that among three bed types the flow over spherical particles exhibits

more coherent structures compared to the flows over randomly packed gravel beds. The PIV data showed that for all bed types there were sporadic ramp structures that extended into the outer flow (and possibly up to the water surface). However, these events did not leave a marked 'imprint' on $\overline{C_{\lambda u}}$, as large-scale zero-crossing interface disappears not far away from $y_{ref}/\delta_h > 0.2$ in figure 5.

4.2. *Horizontal near-bed view*

The signatures of large-scale wedge-like structures from the vertical measurement plane are consistent with flow features revealed from the horizontal measurement plane discussed below. Figure 6 shows typical pictures of streaky structures observed at all three bed types studied. The velocity fields reveal elongated regions of faster and slower flowing fluid (i.e.high- and low-speed streaks), alternating in the spanwise direction. Similar streaky structures have been already noted, e.g. in the flow visualizations of Defina (1996) above a spheres-covered bed, or in the experiments of Nino & García (1996) above a bed roughened by sand particles glued to an originally smooth bed. In figure 6 the described streaky structures are easily recognizable features. These plots suggest that the occurrence of the streaky structures is relatively insensitive to the roughness type, the water depth and the Reynolds number. Among three bed types, however, the streaky structures are most profound above the bed made of spheres (sph1). Although the distance between streaks varies, it most likely scales with the roughness height as was suggested previously in a number of studies (e.g. Grass *et al.* 1991).

The qualitative picture can be made more definite if it is supplemented with quantitative statistical measures. To characterize the streaky structures statistically we used a 'quasi' two-point correlation of u':

$$C_{u_z u}(r_x, z) = \frac{\langle u'(x, z_{ref})\, u'(x + r_x, z)\rangle}{\sigma_u(z_{ref})\, \sigma_u(z)}, \tag{4.3}$$

where $z_{ref} = 0$ is the reference for u'. The correlation function of (4.3) embodies the structural information on the streaks. The dimensions of the region $\overline{C_{u_z u}} > 0$ can be interpreted as the characteristic dimensions of a streak. We found that within $-1.5 < r_x/k_s < 1.5$ the transverse width of $\overline{C_{u_z u}}$ is almost constant along the flow and therefore we used this part of $\overline{C_{u_z u}}$ to define the streak spacing λ_z as the distance between zero crossings of $\overline{C_{u_z u}}$. The resulting values are plotted in figure 7, which are in good agreement with the visualization data from Defina (1996). A linear fit to the whole plotted data set gives

$$\lambda_z = 1.5y + 2.6k_s. \tag{4.4}$$

Equation (4.4) matches the data points quite well, demonstrating that the linear growth of the spanwise length scale with distance from the bed, earlier established for smooth-bed flows by Tomkins & Adrian (2003), is also valid for rough-bed flows. Both Tomkins & Adrian (2003) and Defina (1996) explain the growth mechanism by extended double roller-type vortex structures. However, an unambiguous detection of such eddies from a single horizontal measurement plane is challenging as it may provide information only on vortices whose axes cross the horizontal plane at a reasonably high angle. Unlike Tomkins & Adrian (2003) we were not able to prove (or disprove) the presence of counter-rotating vortices using our data sets.

The application of the same approach of zero crossings for determining the longitudinal dimensions λ_x of the streaks is problematic as the resolved domain

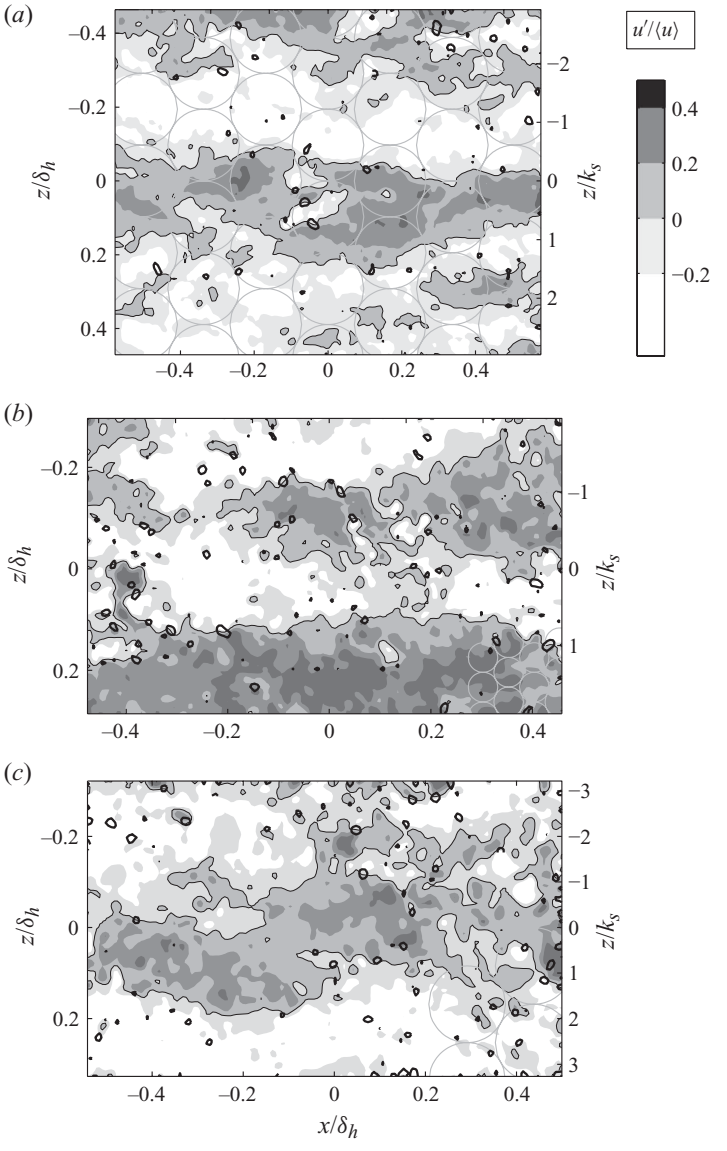

FIGURE 6. Top view of instantaneous velocity fields of $u'/\langle u\rangle$ near the bed. Flow direction is from left to right. Typical pictures of streaky structures can be seen for three different types of bed: (*a*) spheres (sph1, $y_t/k_s = 0.2$), $[y_t, y] = [4.5, 9.5]$ mm; (*b*) uniform gravel (uni6, $y_t/k_s = 0.2$), $[y_t, y] = [5, 7.5]$ mm; and (*c*) Rhine gravel (rhi9, $y_t/k_s = 0.3$), $[y_t, y] = [5, 11.5]$ mm. The velocity fields are filtered by a 3×3 Gaussian filter. Bold contours of swirling strength highlight the location of vortex cores. $u'/\langle u\rangle = 0$ is pronounced by thin lines. The representative grain size d is indicated in the background. The frame sizes are plotted in the same size relation as originally seen by the camera.

of $\overline{C_{u_z u}}$ is not sufficient to exhibit zero crossings in the streamwise direction. However, for approximate estimates of λ_x we can use the aspect ratio of streaks λ_x/λ_z that can be estimated as the ratio of major to minor axes of contour ellipses of $\overline{C_{u_z u}}$. This ratio varies from 3 to 6 and does not depend on the bed type.

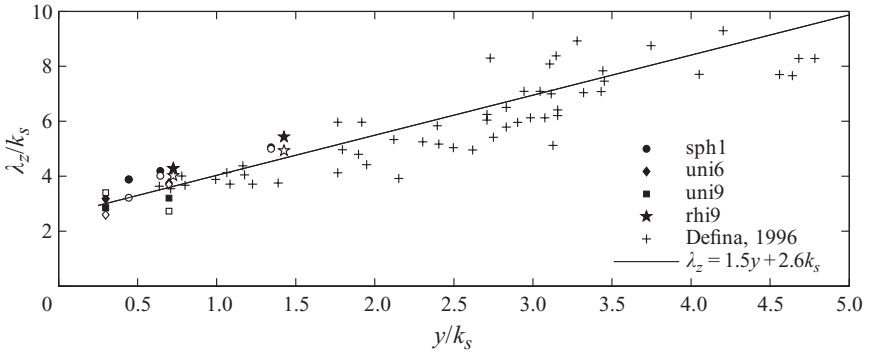

FIGURE 7. Streak spacing λ_z plotted against bed distance y and scaled with k_s. Filled symbols indicate the spacing at $r_x/k_s = 0$ and unfilled symbols indicate the averaged spacing at $r_x/k_s = \pm 1.5$. The figure is supplemented by data from Defina (1996) and a linear fit to the whole plotted data set (see (4.4)).

5. Simultaneous consideration of velocity and pressure fluctuations (event analysis)

5.1. *Time series*

The relation between pressure and velocity fluctuations can be obtained by taking the divergence of the Navier–Stokes equation, leading to the Poisson equation for the fluctuating pressure p'. For an incompressible flow and in a Reynolds-averaged form this equation is (e.g. Chang, Piomelli & Blake 1999)

$$-\frac{1}{\rho}\nabla^2 p' = 2\frac{\partial \overline{u_i}}{\partial x_j}\frac{\partial u_j'}{\partial x_i} + \frac{\partial^2}{\partial x_i \partial x_j}(u_i'u_j' - \overline{u_i'u_j'}). \tag{5.1}$$

The first (linear or mean shear) term on the right-hand side can be defined as the rapid source term since it affects the pressure fluctuation without delay. The second (nonlinear or turbulence–turbulence) term represents the slow source term. Both mean and fluctuation velocity gradients in the entire fluid domain influence p' at a certain moment, but the impact of single sources decreases with distance. It was found by van Radecke & Schulz-DuBois (1988) that the streamwise velocity component u is responsible for most of the pressure variance. If $u > u'$ holds, the product $\overline{u}u'$ is expected to represent the major effect of the fluctuating velocities. Thus, a crude simplification of (5.1) may be written as

$$p'/\rho \approx -\overline{u}u' + C, \tag{5.2}$$

where a constant can be approximated as $C = 0$, if $uu \gg '$ is applicable. Equations (5.1) and (5.2) can serve as a basis for a joint consideration of the measured pressure and velocity fluctuations. As an example, figure 8 shows a synchronous 15 s record of pressure and streamwise velocity for uni6. The head of the MPPS was vertically orientated, and thus a vertical net lift is indicated by $p'/\tau_o < 0$. (Note that supplementary data in Detert (2008) support an assumption that $p' \sim 0$ at the bottom of the first layer of particles, although this approximation may not be universal.) To reveal the significant structure of the pressure signal, the recording was digitally re-sampled from 2125 to 40 Hz using an finite impulse response (FIR) filter. The synchronous PIV measurements were performed in a vertical streamwise plane above the sensor head (set-up A). To better couple pressure fluctuations with velocity fluctuations, the instantaneous term $\overline{u}u'$ in (5.2) was spatially averaged within an

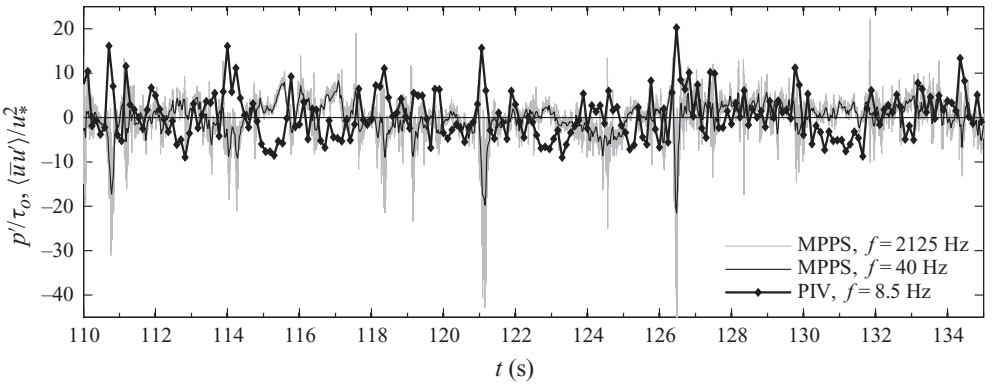

FIGURE 8. Typical synchronous time series of pressure fluctuations p'/τ_o at $y = 0$, together with velocity fluctuations $\langle\overline{u}u'\rangle/u_*^2$ spatially averaged over a vertical streamwise area of $10 \times 7.5\,\mathrm{mm}^2$ above the pressure sensor (uni6). A vertical net lift is indicated by $p'/\tau_o < 0$.

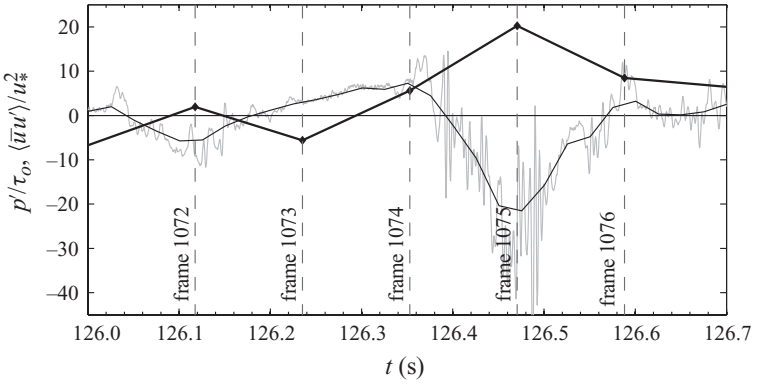

FIGURE 9. Time series of 0.7 s, where a noteworthy pressure drop is recognized (cut-out of figure 8). The vertical dashed lines refer to the corresponding PIV frames 1072–1076.

$x \times y$ window of $10 \times 7.5\,\mathrm{mm}^2$ over the top of the MPPS, and is defined as a quasi-mean-shear term $\langle\overline{u}u'\rangle$. The window size is selected to represent the particle size. The trials with a range of window sizes covering the range of particle sizes showed that the main tendencies described below do not change. Figure 8 shows examples of clear negative correlations between p' and $\langle\overline{u}u'\rangle$, where significant pressure drops occur simultaneously with events of high velocity (e.g. at $t = 110.8$, 121.2 and 126.5 s).

The latter extreme event of low pressure and high streamwise velocity can be better seen in figure 9, which shows a subset $\Delta t = 126$–126.7 s from figure 8. Up to 126.35 s, the pressure increases slowly, from $p'/\tau_o = -6$ to $+8$ within 0.25 s. Then a significant pressure drop can be observed accompanied with superimposed small-scale pressure fluctuations of sharply increased amplitude. In this example, p'/τ_o decreases within 0.12 s from approximately 10 to minimum values around -40, if the small-scale fluctuations are also taken into consideration (the filtered 40 Hz pressure record shows a slightly smaller magnitude). Pressure drops of such kind are favourable with respect to the entrainment of single grains from the bed. Indeed, a force balance considering buoyancy and neglecting friction and inertia shows that -139 Pa (which equals -40 τ_o in figure 9) acting on at least 80 % of the surface of a spherical gravel particle with $d = 10$ mm may exceed the particles' submerged weight.

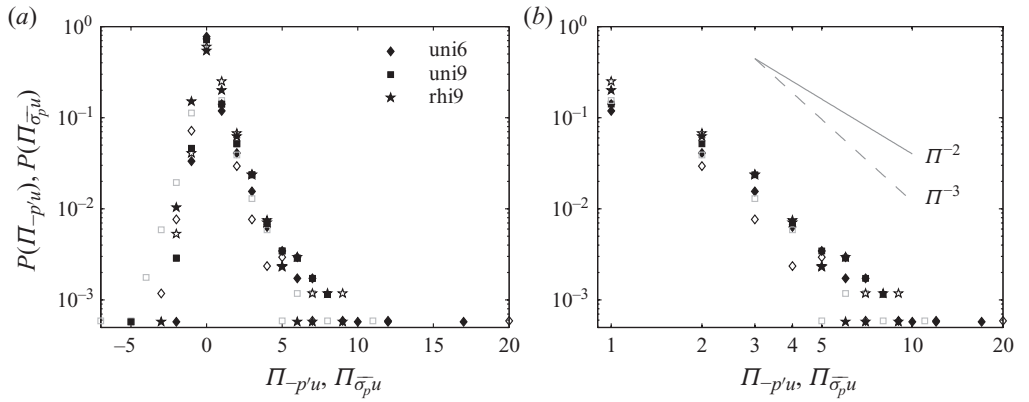

FIGURE 10. The p.d.f.s of the coherence between the pressure and the mean shear term. Unfilled symbols indicate $\Pi_{-p'u}$ and filled symbols indicate $\Pi_{\overline{\sigma_p}u}$. The p.d.f.s in (*a*) are plotted with semi-logarithmic coordinates in order to evaluate both maxima and minima of Π. The p.d.f.s in (*b*) are plotted with logarithmic coordinates to represent the shapes of the positive tails.

Next we will inspect whether these extreme low-pressure zones are typically related to an increased streamwise velocity. Therefore, an instantaneous coherence between the pressure signal and the quasi-mean-shear term is determined in two ways by

$$\Pi_{-p'u} = -\frac{p'\langle\overline{u}u'\rangle(t)}{\sigma(p'\langle\overline{u}u'\rangle)}, \tag{5.3}$$

and

$$\Pi_{\overline{\sigma_p}u} = \frac{{}^{n}\overline{\sigma_p}\langle\overline{u}u'\rangle(t)}{\sigma({}^{n}\overline{\sigma_p}\langle\overline{u}u'\rangle)}, \tag{5.4}$$

where ${}^{n}\overline{\sigma_p}$ denotes the standard deviation of the detrended p within a moving window length of n to get a measure of instantaneous small-scale fluctuations of pressure; denominators in (5.3) and (5.4) represent standard deviations of numerators. The parameter $\Pi_{-p'u}$ gives a measure of the 'instantaneous correlation' of global pressure fluctuations with the quasi-mean-shear term, while $\Pi_{\overline{\sigma_p}u}$ presents the 'instantaneous correlation' between small-scale pressure fluctuations and the quasi-mean-shear term. Note that $\Pi_{-p'u}$ is positive if p' and $\langle\overline{u}u'\rangle$ are correlated negatively, and $\Pi_{\overline{\sigma_p}u}$ gets the sign of u' as ${}^{n}\overline{\sigma_p}$ is positive by definition. The results for the relatively high-Reynolds-number runs uni6, uni9 and rhi9 are plotted as probability density functions (p.d.f.s) in figure 10. Each p.d.f. is based on 1740 values, i.e. the number of PIV frames, with p' FIR-filtered to 40 Hz, ${}^{53}\overline{\sigma_p}$, i.e. σ_p within a time window of 0.025 s, and $\overline{u}u'$ spatially averaged within a spatial window of $10 \times 7.5\,\mathrm{mm}^2$. Both $-p'$ and σ_p show a clear positive correlation to the streamwise velocity. Additionally, we correlated $-p'$ to σ_p in the same manner, which also reveals a clear positive correlation between them (not shown here), similar to figure 10. Thus, one can conclude that on average the events with high streamwise velocity occur simultaneously with significant pressure drops that, in turn, are accompanied by small-scale pressure fluctuations. A closer look at the shapes of the positive tails of $\Pi_{-p'u}$ and $\Pi_{\overline{\sigma_p}u}$ reveals that the probabilities of these extreme events decrease according to power laws, with exponents between -2 and -3.

For relatively low-Reynolds-number flows (sph1) we found that the pressure signals were strongly influenced by the water surface that slightly oscillated with

amplitudes in a sub-millimetre range. The water-surface-induced fluctuations could mask turbulence-induced pressure events and, as a result, no noteworthy pressure drop events were recognizable in the recordings. This fact, however, is most likely because of the effects of the experimental facility and not because of the physical absence of these pressure patterns. For sph1, a further inspection of a correlation between p' and u was omitted. The correlation of pressure with $\langle \overline{u}v' \rangle$ was also reviewed (not shown here) but found to be minor compared to that with $\langle \overline{u}u' \rangle$, as was proposed by van Radecke & Schulz-DuBois (1988).

To correlate the pressure signals with the simultaneously measured velocity fields, the frames 1072–1076 (uni6, figure 9) will be analysed in the next section.

5.2. *Splicing method and spliced flow field*

The view of the large-scale structures through a standard PIV window is limited by the size of the PIV frame, with its length typically comparable to the flow depth. To enlarge the observation window, Hofland (2005) suggested a hybrid technique that involves merging a sequence of PIV frames. Hofland called this technique 'splicing', after the technique used for joining pieces of a rope by interweaving strands. The first step in Hofland's technique is to determine the overlap length between two consecutive PIV frames which covered nearly the whole flow depth in his experiments. This length is defined to be equal to a spatial shift corresponding to the maximum of the two-dimensional cross-correlation function between two images. The obtained spatial lag was then used to move the second image upstream, and then averaging velocity fields within the overlap region, which was throughout $> 2/3$ of the frame length. This operation extends the view in the longitudinal direction by $\sim 1/3$ of the PIV frame length. A similar procedure can be repeated again with the third image, and so on, further extending the standard PIV view in the streamwise direction. This technique is essentially a form of Taylor's 'frozen' turbulence hypothesis, assuming that there is a single convection velocity over the whole flow depth for all structures. In spite of this drawback, Hofland showed that the so-obtained extended views could provide reasonable qualitative and quantitative information on large-scale structures.

Our PIV sampling frequency of 4–8.5 Hz was not as high as in Hofland's 20 Hz experiments and our PIV window covered only approximately 30 % of the flow depth. Therefore, we could not achieve the same degree of overlap between frames and found estimates of the convection velocities from cross-correlation functions to be unreliable. To resolve this problem we have modified the described procedure by estimating the overlap length as

$$\Delta x_{shift} = \frac{\langle u_1 \rangle + \langle u_2 \rangle}{2} \, \Delta t_{PIV}, \tag{5.5}$$

where $\langle u_1 \rangle$ and $\langle u_2 \rangle$ denote the frame-averaged velocities of the two successive PIV frames. Then, the extension procedure suggested by Hofland was applied. Figure 11 provides an example of five separate frames and the resulting spliced velocity field, referring directly to the time series presented in figure 9. A key feature is that the strong similarities of the overlapping regions visible on the images are mainly due to the large-scale structures, while small-scale features quickly change, as one would expect.

Before we proceed with the analysis of flow structures using spliced flow fields it is useful to comment on the reliability of the splicing procedure. For this we use the

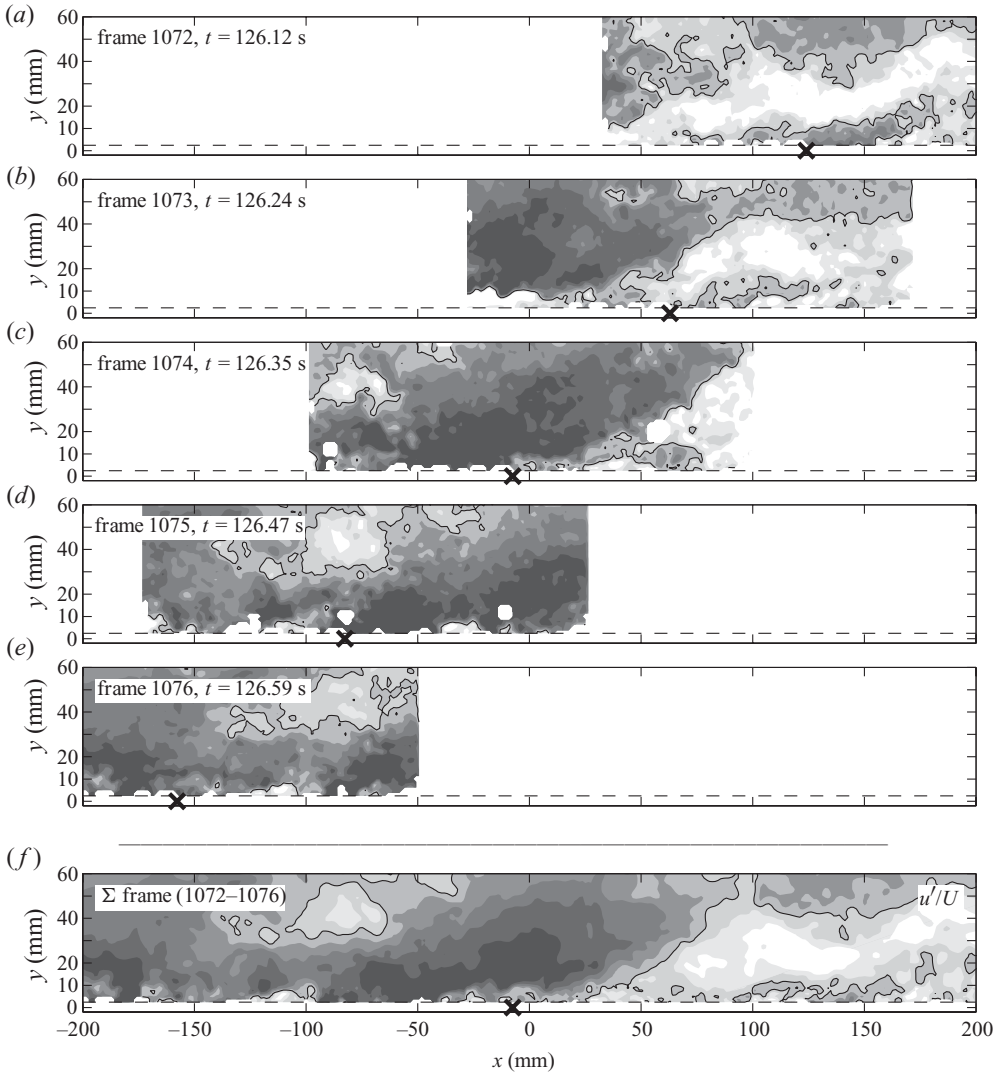

FIGURE 11. (*a–e*) Five original images of $u'(x, y)$, together with (*f*) the spliced image obtained from them. The single frames were smoothed by a 3×3 Gaussian filter and the spliced image was further smoothed by a 3×3 moving average filter. The shading indicates u'/U in steps of 0.1 (colourbar: see figure 4) and the isoline denotes $u'/U = 0$. The crosses refer to the position of the pressure sensor, whose measured signal is given in figure 8.

correlation coefficient r_{12} between the overlapping regions, which is defined as

$$r_{12} = \frac{\sum_m \sum_n u'_{1,mn} u'_{2,mn}}{\sqrt{\left(\sum_m \sum_n (u'_{1,mn})^2\right)\left(\sum_m \sum_n (u'_{2,mn})^2\right)}}. \tag{5.6}$$

For an example in figure 11, the values of this coefficient ($r_{12} = [0.65, 0.74, 0.73, 0.79]$) are smaller than ideal (=1.0), reflecting a de-correlation effect of quickly evolving small-scale features. Large-scale structures, however, are well captured and

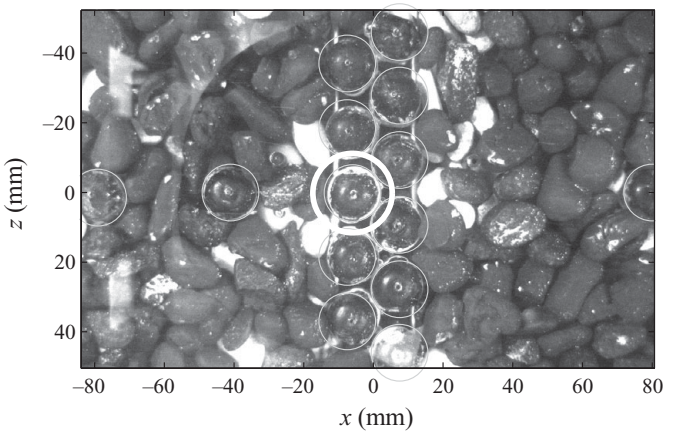

FIGURE 12. Top view of the MPPS mounted in the gravel layer, here in the arrangement as used for synchronous PIV measurements of set-up B. The white circle highlights the target sensor head at $[x, y, z] = [-6.0, -1.5, 0.2]$ (mm). The size of the frame is exactly the same as in figure 6(*b*).

thus the obtained spliced flow fields can serve for our analysis. Field (Nikora & Goring 2000) and laboratory tests (Dennis & Nickels 2008) provide additional support to this conclusion.

Now, we can take a closer look at the flow structure shown in figure 11. Starting with $t = 126.12$ s (frame 1072), the key feature of the velocity field is a slow-flowing fluid region inclined at an angle of approximately 20° (elongated white spot). Keeping its wedge-like structure, the region moves forwards, followed by a larger fast-flowing fluid region ($t = 126.24$–126.47 s, frames 1073–1075, elongated dark spot). Due to its higher propagation velocity, the second fluid region overruns the first one. As a result of differences in velocities a shear layer between these regions is developed and populated with small eddies. (This is better seen in figure 4(*b*), where frame 1073 is shown.) At $t = 126.47$ s (frame 1075), the lower velocity region of the flow completely left the actual frame. As one can deduce from figure 9, p' drops significantly when the tail of the slower wedge-like fluid structure has passed the location of the pressure sensor and the faster fluid zone becomes dominant. Thus, the pressure drop measured at this flow event is strongly correlated with a passage of a high-speed fluid with increased near-bed streamwise velocity. This in turn indicates that the measured pressure drop at this event is mainly due to a Bernoulli-akin effect resulting from the interaction between the two fluid packets. The associated small-scale pressure fluctuations visible in figure 9 are probably due to the effects of eddy shedding or eddies generated at the shear interface of the two fluid zones, as has been highlighted in Mignot, Hurther & Barthelemy (2009).

In the next section, the splicing method will be applied to analyse both velocity and pressure fields and to identify typical patterns of interactions between them.

5.3. *Synoptic view*

The pressure time series in our experiments were recorded simultaneously by an array of up to 15 MPPS. If Taylor's frozen turbulence hypothesis is assumed to be applicable to pressure as well, then spatial footprints of pressure fields can be reconstructed from these point measurements. During the synchronous PIV–MPPS measurements, the pressure sensors were typically arranged in an array, as shown in figure 12 (see also

figure 2*b*). The time signals of the 11 MPPS located at $-8\text{ mm} < x < 8\text{ mm}$ can be used to reconstruct pressure fields by applying Taylor's hypothesis of frozen turbulence, i.e.

$$x_\lambda = -U_c t, \tag{5.7}$$

where U_c denotes the mean convection velocity of the pressure field. To obtain its value, we first tried the standard approach when U_c is defined as a ratio of the distance between two pressure probes aligned along the flow to the time shift corresponding to the maximum in the time cross-correlation function between the probes. For low-Reynolds-number flows (sph1) we found that the obtained convection velocity $U_c \propto \sqrt{(gh)} > U$, indicating that (surface) waves passing by had a strong influence on the bed-pressure fluctuations and were the main contributors to the correlation peak. For high-Reynolds-number flows (uni6, uni9 and rhi9) we obtained $U_c = (0.6\text{–}1.0)\,U$, indicating that the dominant events in the pressure fields propagate with the near-bed velocities and are most likely generated by passing large-scale structures. To avoid confusing results due to potential 'contamination' of pressure signals with the surface-waves effects we selected to estimate U_c as the actual frame-averaged velocity $\langle u \rangle$. Thus, we used the same convection velocity for both pressure and velocity fields, allowing their consistent coupling.

As an example, figure 13 shows realizations of pressure and velocity fields reconstructed from experimental data for the high-Reynolds-number experiment uni6, where simultaneous MPPS–PIV measurements were performed (set-up A for PIV). The observed patterns provide further support to the strong coupling between pressure and velocity fields that has been already highlighted in figures 8 and 9. The synoptic view of the flow in these figures is presented by (i) velocity vector field (upper plot), (ii) fields of $v'\overline{u}$ and $u'\overline{u}$ (two lower plots) and (iii) bed-pressure field (bottom plot). To reconstruct the bed-pressure field in figure 13, $U_c = 0.91\,U$ was adopted as the mean streamwise velocity of the spliced velocity field. Due to the finite dimensions of the sensor heads, an array of 11 MPPS had to be arranged in two lateral alignments, 5 and 6 MPPS in each alignment. The longitudinal lag in the MPPS alignments, defined by crosses in the bottom plot, was accounted for by shifting the spatial reconstruction of six downstream MPPS upstream. Each pressure signal was first FIR-filtered to 200 Hz, and then the reconstructed spatial fields were additionally smoothed with a 3×3 Gaussian filter. As a result, the small-scale details in the pressure fields were filtered out, to keep consistency with the spliced velocity fields which have been smoothed in a similar way. While interpreting figure 13, it should be kept in mind that the flow direction is from left to right, whereas the time increases from right to left.

There are two distinct regions in the pressure field shown in figure 13(*d*): an elongated and slightly bent high-pressure domain within $x_\lambda = -20$ to $+100$ mm, and an adjacent low-pressure domain at $x_\lambda = -150$ to -40 mm, which is approximately elliptical in shape. Comparing the pressure field in the bottom plot with the velocity field ($\overline{u}u'$) in the upper plot one can note that the high-pressure region is located directly under the decelerated velocity zone, with the low-pressure region being under the high-speed velocity zone. The extrapolation of the interfacial shear layer towards the bed indicates the transition between the high- and low-pressure regions. These features suggest that the Bernoulli-akin effect is the main cause of the extreme pressure drop and the structural appearance of the (reconstructed) pressure field. In contrast to $\overline{u}u'$, the field of $v'\overline{u}$ reveals no distinctive features in the near-bed region, suggesting that $v'\overline{u}$ must be of minor importance for the genesis of the large-scale structure of the

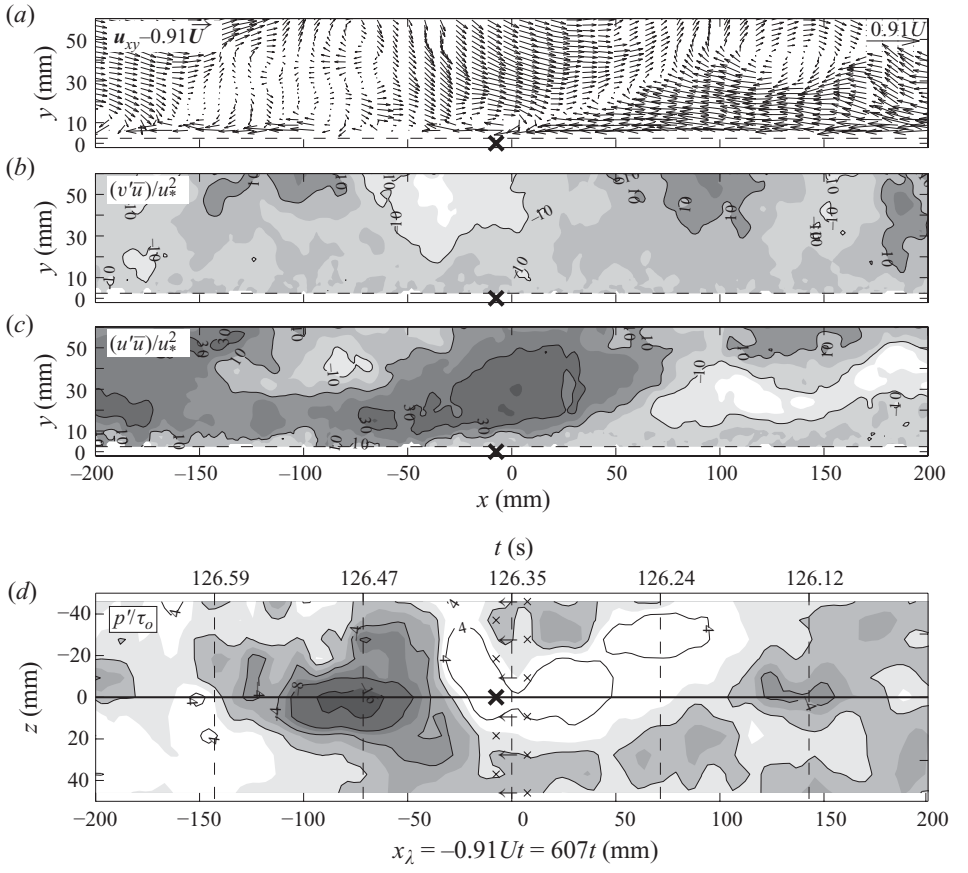

FIGURE 13. Synoptic view of (*a–c*) the spliced velocity field in a streamwise vertical plane and (*d*) the corresponding reconstructed bed-pressure fluctuations (uni6) at $y = 0$ (plan view); the horizontal line marks the PIV axis. The visualization gives a spatial view of the extreme pressure drop event, as shown in figure 9.

pressure field. This is unexpected, as the low-pressure region is normally associated with a noticeable upwelling, and thus one would expect a strong vertical velocity that is seen. The spliced vector field (figure 13*a*) clearly reveals two velocity zones and a typical inclined shear layer between them, already highlighted in figures 3–5. At the upper end of this interface, there is a striking feature – a clockwise-rotating eddy. (Its distorted elliptical appearance is most likely due to the drawbacks of the splicing procedure.) The vortex diameter can be estimated to be in the range (0.25–0.30) h. Its origin and connection to the high- and low-momentum-flow regions are not fully clear. For example, it could be interpreted as a large-scale roller in the sense of Shvidchenko & Pender (2001). On the other hand, it can also be interpreted as the oversized head of a hairpin vortex, in the sense of Adrian *et al.* (2000*b*).

The flow-pressure patterns similar to those shown in figure 13 for run uni6 are also typical for the other high-Reynolds-number runs uni9 and rhi9, as illustrated in figures 14 and 15, respectively. In figure 14, two coupled high- and low-pressure patterns can be seen clearly. The first pattern at $x_\lambda = -140$ to -20 mm is located around the centreline of the measurement window with the PIV plane crossing it precisely through the centre. Its correlation with the velocity field is the same as

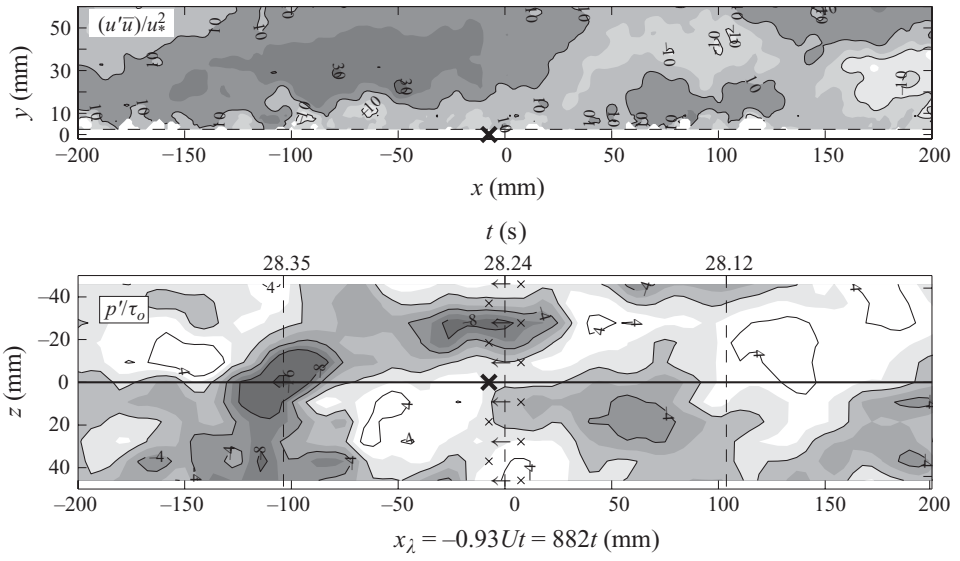

FIGURE 14. uni9; for further caption see figure 13.

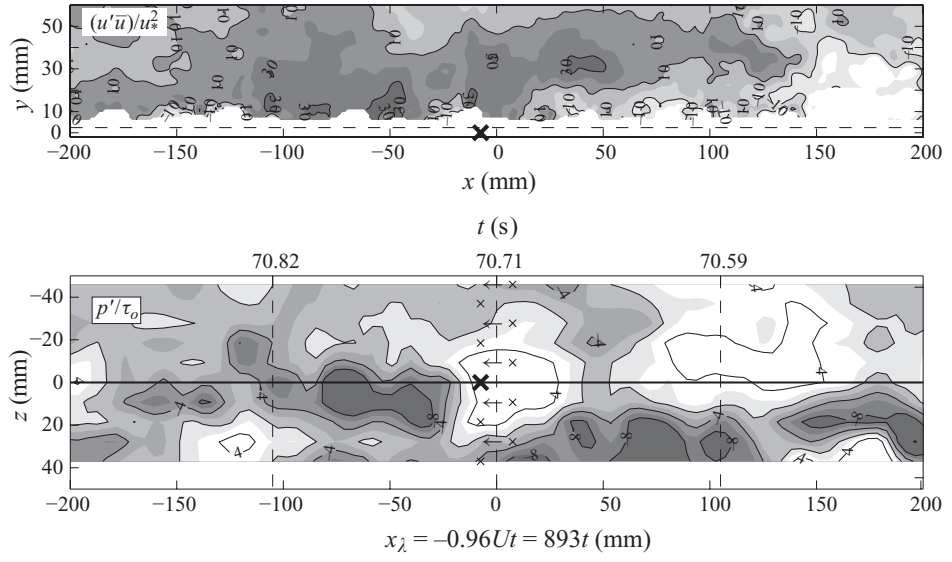

FIGURE 15. rhi9; for further caption see figure 13.

in figure 13. The second high- and low-pressure pattern at $x_\lambda = -50$ to $+60$ mm is located outside the PIV plane at $z = -10$ to -40 mm, and thus no direct reference can be given to the recorded velocity field. Figure 15 for rhi9 reveals features similar to those highlighted in figures 13 and 14, as can be seen at $x_\lambda = -100$ to $+30$ mm. Comparing figures 14 and 15 to figure 13 one may conclude that the patterns of high- and low-pressure regions at the water–sediment interface typically scale with the water depth and have elongated shapes.

Similar to figures 13–15, plain views of bed-pressure fluctuations were also obtained for the low-Reynolds-number experiments with the spheres-covered bed

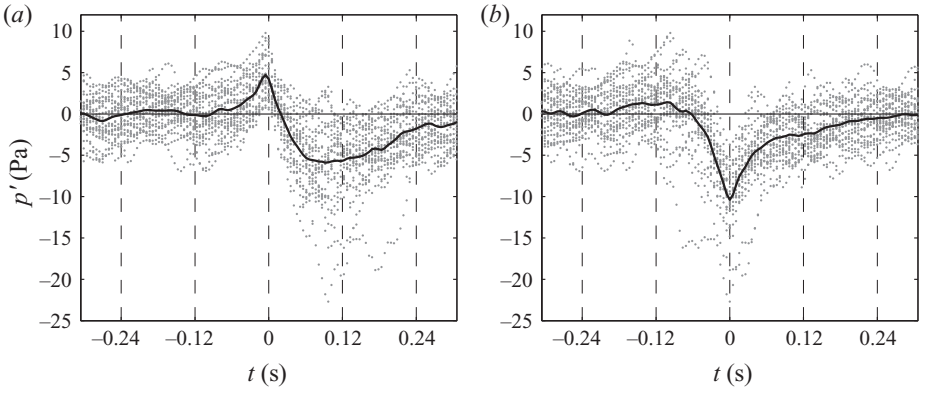

FIGURE 16. Ensemble-averaged time history of 25 essential pressure drops (lift), uni6. Measured at $y = 0$ synchronous to 1740 PIV recordings ($8.5\,\mathrm{Hz} = 1/0.12\,\mathrm{s}^{-1}$). Conditionally sampled by association with (*a*) maximum peak and (*b*) minimum trough.

(i.e. sph1). However, these views revealed that at such bed and flow conditions the pressure measurements were strongly dominated by the influence of the water-surface oscillations that occurred with sub-millimetre amplitudes. Their 'contaminating' effect precluded, most likely, a clear identification of pressure patterns similar to those shown in figures 13–15. For this reason run sph1 will also not be considered in the following subsection.

5.4. *Conditional averaging*

A qualitative picture discussed in the previous subsection highlighted that the large-scale events in the flow most likely have strong footprints in the fluctuating bed-pressure field. In particular, the boundary between the low- and high-pressure domains is typically associated with the footprint of the interfacial shear layer between high- and low-momentum regions. The observed sudden decreases in the bed pressure appear to be strongly correlated with a passage of a high-speed fluid with increased near-bed streamwise velocity, akin to a Bernoulli lift with a missing obstacle. To reduce potential subjectivity in these qualitative observations, some quantitative measures should be implemented that would allow quantification of the noted effects. The conditional sampling and averaging seems to be the most appropriate step towards this goal.

Figure 16 shows, as an example, an ensemble average of pressure-drop patterns, conditionally sampled using maximum peaks (*a*) and minimum troughs (*b*) as characteristic points. A conditional sampling procedure included the following steps. First, the pressure signal of the 'target' pressure sensor was FIR-filtered to 200 Hz. Then $\mathrm{d}p_{200\,\mathrm{Hz}}/\mathrm{d}t$ was computed and smoothed by a moving averaging window of length $n = 20$ to weaken the influence of potential spikes. The resulting signal

$$C = \overline{\mathrm{d}p_{200\,\mathrm{Hz}}/\mathrm{d}t}^{\,20} \tag{5.8}$$

was used to detect events of 'steep' changes in the pressure fluctuations. For the plots in figure 16, we have chosen $C = -0.75$ as a threshold value; so events with only lower values of C have been selected as 'events'. The threshold $C = -0.75$ was identified from a range of values after initial trials as it provided the clearest patterns. As a result, 25 events were sampled within a time series of 205 s. Finally, the selected events were superimposed and then ensemble-averaged using two alternative

approaches: (i) by superimposing maximum peaks and (ii) by superimposing minimum troughs. A closer look at the plots in figure 16 shows that the ensemble average based on the 'minimum-trough' approach highlights features different from those seen in the pattern based on the 'maximum-peak' approach. In the latter, $p' > 0$ lasts, on average, < 0.12 s, whereas the duration of $p' < 0$ is about twice this value. A similar ratio is noted for $|p'_{min}/p'_{max}| \approx 2$. This skewness in the pressure pattern could be expected, and it confirms the pressure dependence on the squared near-bed velocity, as recently discussed in Hofland & Battjes (2006). (Note that the distribution of a normally distributed variable with a non-zero mean, here the near-bed velocity, gets skewed if it is squared.)

The selected pressure events can now be used to identify the associated velocity fields (PIV frames) and then by averaging these fields to obtain an average pattern of the related flow structure. This was achieved by re-sampling PIV frames corresponding to the closest time moments when pressures were measured, and then slightly shifting them for synchronization by

$$\Delta x_{cd} = \langle u \rangle (t_{p\text{-}drop} - t_{PIV}), \tag{5.9}$$

where Δx_{cd} denotes the 'spatial-re-sample' correction of the velocity field, $\langle u \rangle$ is the streamwise frame-averaged velocity, $t_{p\text{-}drop}$ is the event time of p'_{max} and t_{PIV} is the real time of the nearest PIV frame. After this procedure had been completed, the flow field was spliced and finally filtered twice by a 3×3 moving average filter to facilitate interpretation.

Figure 17 illustrates the resulting averaged flow field in the xy plane, together with the associated averaged bed-pressure field (uni6). This figure provides a strong statistical support to the qualitative considerations presented in the preceding subsections which were mainly based on the selected instantaneous patterns. The statistically averaged flow pattern can be summarized as follows. A fast large-scale fluid region overruns a slower low-momentum region below it. These regions are separated by an interfacial shear zone inclined to the bed at approximately 20° in the streamwise direction. As the tail of the high-momentum region is in the direct vicinity of the bed, its streamwise component, u' in figure 17, causes a lift effect at the bed – akin to a Bernoulli lift. The vertical flow component, v' in figure 17, seems to be of minor importance to this mechanism. The streamwise extension of the faster fluid region is in the range of one to two flow depths while its vertical size reaches at least a half flow depth. The low- and high-bed-pressure zones, induced by large-scale flow structures, have longitudinal dimensions comparable to the flow depth, whereas their lateral extension is in the range of 2–4 k_s, consistent with the lateral streak spacing in figure 7 and (4.4).

Figure 18, showing ensemble-averaged patterns obtained using the PIV set-up B, indeed supports the above picture. The reconstructed conditionally averaged bed-pressure field in figure 18 well resembles the corresponding pattern in figure 17, highlighting the reliability of the identified pattern. Note that both patterns represent averaging nearly the same number of individual events (25 and 24). However, the averaged flow fields are subjected to a large scatter. Two reasons may explain this scatter: (i) the measurements were performed with a lower frame rate and thus the 'nearest-neighbour' shift Δx_{cd} in (5.9) is larger, leading to additional errors in 'corrected' PIV frames, and (2) the instantaneous streaks revealed a tendency for meanderingly (not shown) adding additional scatter effect into the averaged pattern. Consequently, an ensemble-averaged horizontal field can be more strongly biased by extreme deviations than a streamwise vertical field. Nevertheless, the resulting

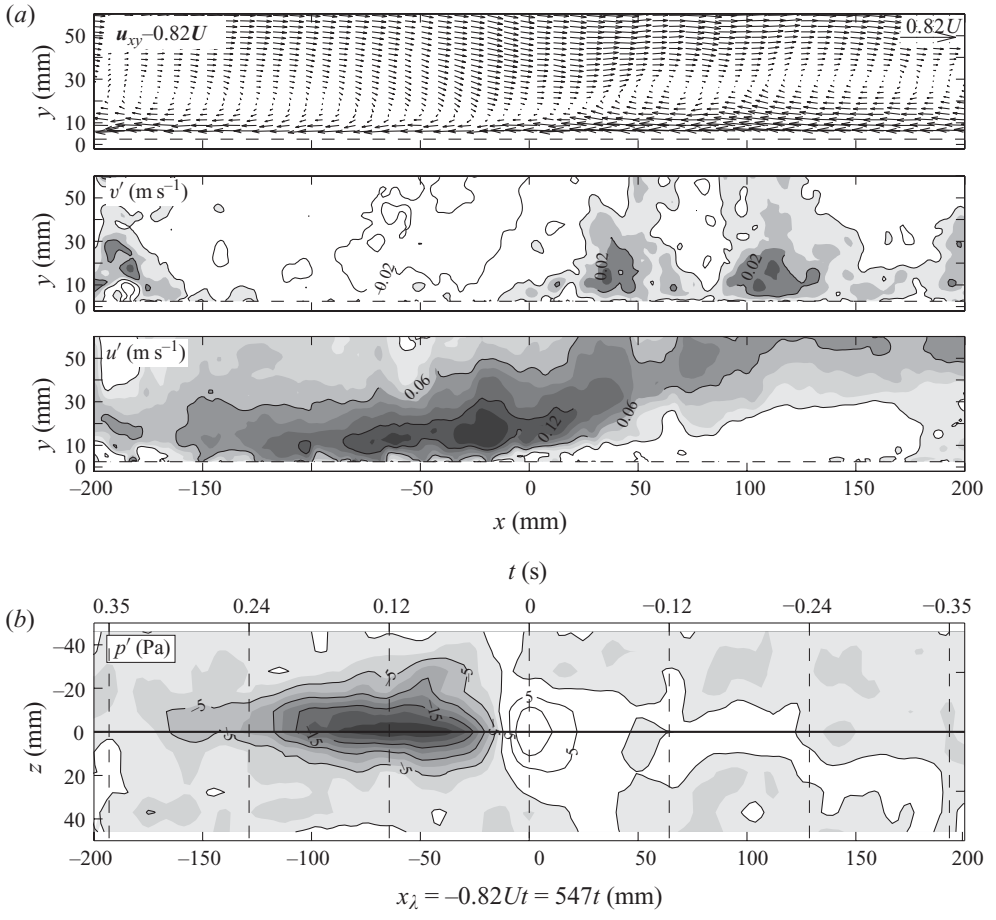

FIGURE 17. Ensemble average of (*a*) the near-bed spliced velocity field in a streamwise vertical plane (flume centreline) (side view) and (*b*) the corresponding reconstructed bed-pressure field at $y = 0$ mm (uni6). From 25 spliced PIV frames that were conditionally sampled (maximum-peak approach) from the corresponding 25 most essential pressure drops (criteria: $C \leqslant -0.75$). The velocity field was finally filtered twice by a 3×3 moving average filter to facilitate interpretation. Due to 'maximum-peak' sampling, the distinctiveness of the low-pressure field is weakened.

horizontal field of the streamwise velocity component agrees quite well with the related streamwise vertical fields discussed above. The longitudinal extensions of horizontal structures scale with the flow depth, as expected, while its lateral extensions correlate with the dimensions of the bed-pressure field structures. The transverse-velocity field suggests that the downstream part of the faster fluid zone spreads away from the centreline, whereas the upstream part of the structure tends towards the centreline, a process also observed in smooth-wall turbulent boundary layers.

The same ensemble averaging procedure as used in the analysis of run uni6 was also done for uni9 and rhi9. The results (not shown here) confirm the principal findings illustrated in figures 17 and 18, suggesting that the identified flow-pressure patterns are relatively independent of the bed structure. However, the depiction of the spliced and averaged velocity fields for runs uni9 and rhi9 suffers from a larger scatter than the depiction for uni6, probably reflecting the effects of the overlap length between the spliced PIV frames.

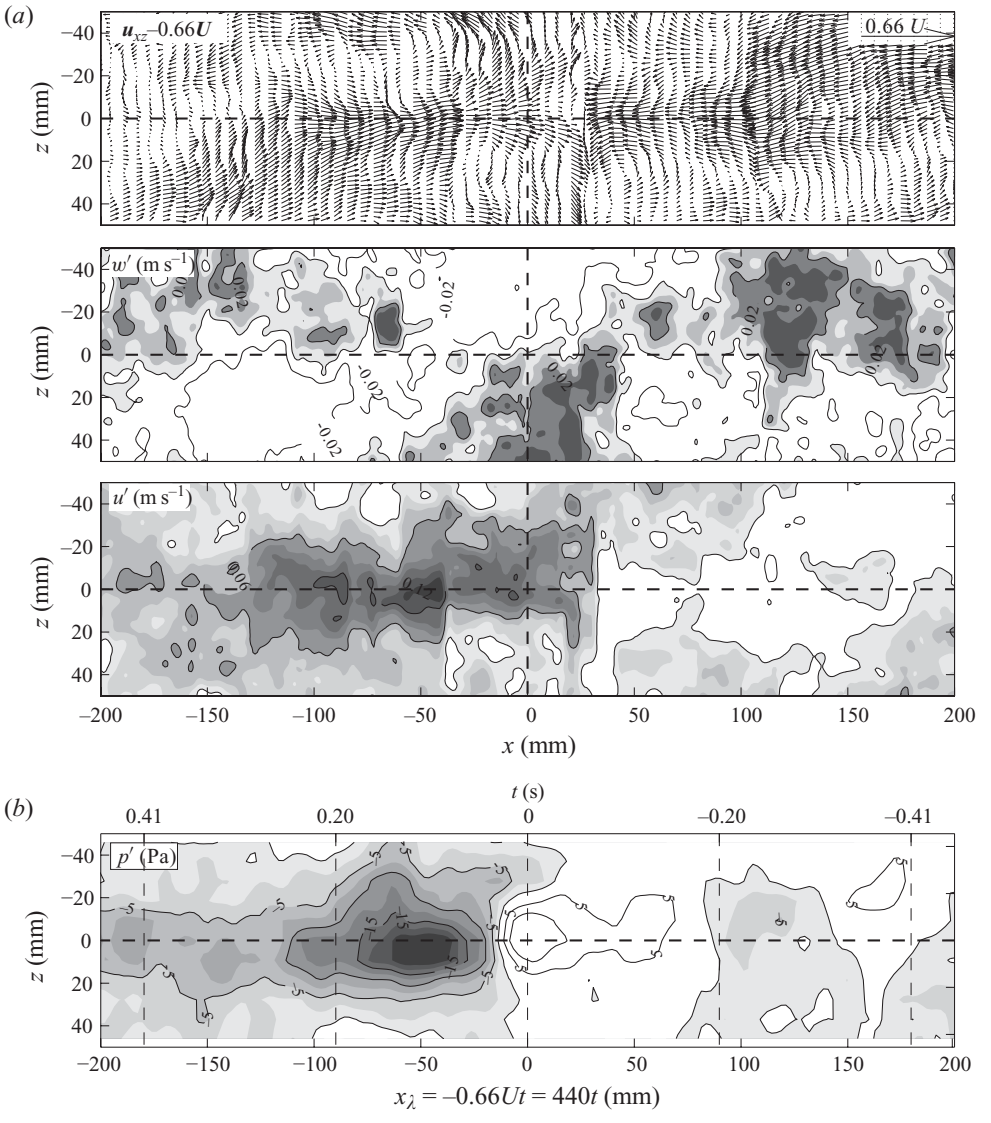

FIGURE 18. Ensemble average of (*a*) the near-bed spliced velocity field in a horizontal plane at $y = 8$ mm (top view) and (*b*) the corresponding reconstructed bed-pressure field at $y = -2$ mm (uni6). From 24 spliced PIV frames that were conditionally sampled (maximum-peak approach) and corresponded to 24 most essential pressure drops (criteria: $C \leqslant -0.75$). The velocity field was finally filtered twice by a 3×3 moving average filter. Due to 'maximum-peak' sampling, the distinctiveness of the low-pressure field is weakened.

6. Summary and discussion

The key findings of our experimental study of open-channel flows over three types of permeable granular beds and associated bed pressure fluctuations can be summarized as follows:

(i) Two-dimensional PIV measurements in a streamwise vertical plane revealed large-scale wedge-like flow structures consisting of a high-momentum fluid region (resembling a sweep, i.e. $u' > 0, v' < 0$), which over-rolls a low-momentum fluid region (resembling an ejection, i.e. $u' < 0, v' > 0$). The interfacial shear layer between

these regions is inclined to the bed at an angle of 10°–25° and populated with clockwise rotating eddies. On average, this pattern occurs with sufficient frequency and shape, and can be conditionally sampled and then ensemble-averaged. Typically, this flow pattern forms near the bed, occupying the logarithmic layer and occasionally extending above it, sometimes up to the water surface. The described pattern appears to be typical for all studied granular bed types and is insensitive to the Reynolds number for a studied range (20 000–200 000).

(ii) Two-dimensional PIV measurements in a near-bed horizontal plane revealed that the flow field is structured with 'chessboard' elongated patches of high and low velocities. The lateral extension of these streaky structures is typically two to four times the equivalent sand roughness k_s, and it increases linearly with distance from the bed. The length of these elongated structures reaches up to several flow depths. In the shear zones between the streaky structures, horizontally rotating eddies are visible, although their occurrence is not always detectable. These horizontal features are typical for all studied beds and largely insensitive to variations in the Reynolds number.

(iii) The bed-pressure fluctuations p' and the 'quasi'-mean-shear source term $u'\overline{u}$ are correlated negatively. Typically, the high-pressure fields are located directly under decelerated velocity zones and low-pressure fields lie under high-velocity zones. Consequently, the lift akin to a Bernoulli lift is considered to be the main cause of extreme pressure drops and the structural appearance of the bed-pressure field. Unlike $u'\overline{u}$, the term $v'\overline{u}$ reveals no distinctive features in the near-bed region which would correlate with the bed-pressure features. Thus, $v'\overline{u}$ must be of minor importance to the genesis of the large-scale pressure patterns.

Some of the flow properties similar to those summarized above have been earlier highlighted for smooth-wall flows in studies of Adrian and colleagues (e.g. Adrian *et al.* 2000*b* and Tomkins & Adrian 2003), which are reviewed in Adrian (2007). Indeed, although two-dimensional PIV measurements cannot provide fully three-dimensional patterns, they reveal two-dimensional features which are fully consistent with the HVP discovered for smooth-wall flows. This suggests that Adrian and coworkers' model should also be applicable for flows over hydraulically rough granular permeable beds. In this respect, our study supplements and further extends the work of Hurther *et al.* (2007), which was based on acoustic Doppler profiler measurements and mainly concerned with the outer flow layer. Based on our experiments, an important additional feature that can be added to the HVP model is its connection to associated variations in the bed-pressure field. Our findings on flow structures are also consistent with the data reported for rough-bed open-channel flows in Defina (1996), Buffin-Bélanger, Roy & Kirkbride (2000), Shvidchenko & Pender (2001), Roy *et al.* (2004), Hofland (2005), Stösser *et al.* (2005) and Hurther *et al.* (2007). As for our bed-pressure results, it is interesting to recall the study of Thomas & Bull (1983), who found a strong correlation between the (smooth-)wall pressure fluctuation and the ramp-like velocity pattern moving above.

Our findings have direct implications for sediment transport, particularly for particle entrainment. The reconstructed bed-pressure fields indicate that bed particles are generally subjected to an uplift when a near-bed sweep event dominates the flow in the particle neighbourhood. Thus, an additional lift due to a vertical upward velocity is not necessarily required to raise a particle; so it can be moved away. This was probably observed in Cameron's (2006) experiments who found that particle entrainment was mainly associated with large-scale sweep events. We can conclude that the structural features of the flow–bed interaction, revealed in our experiments,

can be considered as representative for channel-flow processes and may help in advancing the long-standing problem of sediment transport.

Support by the 'Baden-Württemberg Research Program Securing a Sustainable Living Environment' (BWPLUS, project BWR 25003) with funds of the State of Baden-Württemberg is gratefully acknowledged. The work was also partly supported by the DFG, Germany (JI 18/19-1), and EPSRC, UK (EP/G056404/1), within the project 'High-resolution numerical and experimental studies of turbulence-induced sediment erosion and near-bed transport'. A more complete data source is given in the thesis of Detert (2008).

REFERENCES

Adrian, R. J. 2007 Hairpin vortex organization in wall turbulence. *Phys. Fluids* **19**, 1–16.

Adrian, R. J., Christensen, K. T. & Liu, Z. C. 2000*a* Analysis and interpretation of instantaneous turbulent velocity fields. *Exp. Fluids* **29**, 275–290.

Adrian, R. J., Meinhart, C. D. & Tomkins, C. D. 2000*b* Vortex organization in the outer region of the turbulent boundary layer. *J. Fluid Mech.* **422**, 1–54.

Bowen, L. & Radin, C. 2003 Packing of equal spheres in hyperbolic space. *Discrete Comput. Geom.* **29**, 2339.

Buffin-Bélanger, T. & Roy, A. 2005 1 min in the life of a river: selecting the optimal record length for the measurement of turbulence in fluvial boundary layers. *Geomorphology* **68**, 77–94.

Buffin-Bélanger, T., Roy, A. & Kirkbride, A. D. 2000 On large-scale flow structures in a gravel-bed river. *Geomorphology* **32**, 417–435.

Buffington, J. M. & Montgomery, D. R. 1997 A systematic analysis of eight decades of incipient motion studies, with special reference to gravel-bedded rivers. *Water Resour. Res.* **33** (8), 1993–2029.

Cameron, S. M. 2006 Near-boundary flow structure and particle entrainment. PhD thesis, University of Auckland.

Cameron, S. M., Coleman, S. E., Melville, B. W. & Nikora, V. I. 2006 Marbles in oil, just like a river? In *River Flow 2006* (ed. R. Ferreira, E. Alves, J. Leal & A. Cardoso). Taylor & Francis.

Carman, P. C. 1956 *Flow of Gases Through Porous Media*. Butterworth Scientific.

Chang, P. A., Piomelli, U. & Blake, W. K. 1999 Relationship between wall-pressures and velocity-field sources. *Phys. Fluids* A **11** (11), 3434–3448.

Christensen, K. T. & Adrian, R. J. 2001 Statistical evidence of hairpin vortex packets in wall turbulence. *J. Fluid Mech.* **431**, 433–443.

Defina, A. 1996 Transverse spacing of low-speed streaks in a channel flow over a rough bed. In *Coherent Flow Structures in Open Channels* (ed. P. J. Ashworth, S. L. Bennett, J. L. Best & S. J. Mc Lelland). John Wiley & Sons.

Dennis, D. J. C. & Nickels, T. B. 2008 On the limitations of Taylor's hypothesis in constructing long structures in a turbulent boundary layer. *J. Fluid Mech.* **614**, 197–206.

Detert, M. 2008 Hydrodynamic processes at the water–sediment interface of streambeds. Doctoral thesis, University of Karlsruhe, available at: http://digbib.ubka.uni-karlsruhe.de/volltexte/1000008267

Drake, T., Shreve, R., Dietrich, W., Whiting, P. & Leopold, L. 1988 Bed load transport of fine gravel observed by motion-picture photography. *J. Fluid Mech.* **192**, 193–217.

Grass, A. J., Stuart, R. J. & Mansour-Tehrani, M. 1991 Vortical structures and coherent motion in turbulent flow over smooth and rough boundaries. *Phil. Trans. R. Soc. A: Math. Phys. Engng Sci.* **336**, 36–65.

Hardy, R. J., Best, J. L., Lane, S. N. & Carbonneau P. E. 2009 Coherent flow structures in a depth-limited flow over a gravel surface: the role of near-bed turbulence and influence of Reynolds number. *J. Geophys. Res.* **114**, 1–18.

HAZEN, A. 1892 Physical properties of sands and gravels with reference to use in filtration. *Rep.* 539, Massachusetts State Board of Health.

HEAD, M. R. & BANDYOPADHYAY, P. 1981 New aspects of boundary layer structure. *J. Fluid Mech.* **107**, 297–338.

HOFLAND, B. 2005 Rock & roll. PhD thesis, TU Delft, available at: www.library.tudelft.nl

HOFLAND, B. & BATTJES, J. A. 2006 Probability density function of instantaneous drag forces and shear stresses on a bed. *J. Hydraul. Engng* **132** (11), 1169–1175.

HOFLAND, B. & BOOIJ, R. 2004 Measuring the flow structures that initiate stone movement. In *River Flow 2004* (ed. M. Greco, A. Carravetta & R. Della Morte). A. A. Balkema.

HOFLAND, B., BOOIJ, R. & BATTJES, J. A. 2005 Measurement of fluctuating pressures on coarse bed material. *J. Hydraul. Engng* **131** (9), 770–781.

HURTHER, D., LEMMIN, U. & TERRAY, E. A. 2007 Turbulent transport in the outer region of rough-wall open-channel flows. *J. Fluid Mech.* **574**, 465–493.

JACKSON, G. 1976 Sedimentological and fluid-dynamic implications of the turbulent bursting phenomenon in geophysical flows. *J. Fluid Mech.* **77**, 531–560.

KLINE, S. J., REYNOLDS, W. C., SCHRAUB, F. A. & RUNSTADLER, P. W. 1967 The structure of turbulent boundary layers. *J. Fluid Mech.* **30**, 741–773.

MEYER-PETER, E. & MÜLLER, R. 1949 Eine Formel zur Berechnumg des Geschiebetriebs. *Schweiz. Bauzeitung* **67** (3), 29–32.

MIGNOT, E., HURTHER, D. & BARTHELEMY, E. 2009 Double averaging analysis and local flow characterization of near bed turbulence in gravel-bed channel flows. *J. Fluid Mech.* **618**, 279–303.

NELSON, J. M., SHREVE, R. L., MACLEAN, S. R. & DRAKE, T. G. 1995 Role of near-bed turbulence structure in bed load transport and bed form mechanics. *Water Resour. Res.* **31** (8), 2071–2086.

NEZU, I. & NAKAGAWA, H. 1993 *Turbulence in Open-Channel Flows*. A. A. Balkema.

NIKORA, V. I. & GORING, D. G. 2000 Eddy convection velocity and Taylor's hypothesis of frozen turbulence in a rough-bed open-channel flow. *J. Hydrosci. Hydraul. Engng* **18** (2), 75–91.

NIKORA, V. I., GORING, D. G., MACEWAN, I. & GRIFFITHS, G. 2001 Spatially averaged open-channel flow over rough bed. *J. Hydraul. Engng* **127** (2), 123–133.

NINO, Y. & GARCÍA, M. H. 1996 Experiments on particle–turbulence interactions in the near wall region of an open channel flow: implications for sediment transport. *J. Fluid Mech.* **326**, 285–319.

VAN RADECKE, H. & SCHULZ-DUBOIS, E. O. 1988 Linear response of fluctuating forces to turbulent velocity components. In *Proceedings of the Fourth International Symposium on Applications of Laser-Doppler Anemometry to Fluid Mechanics* (ed. R. J. Adrian), pp. 23–44. Lisbon, Portugal, Springer.

VAN RIJN, L. C. 1984 Sediment transport. Part I. Bed load transport. *J. Hydraul. Engng* **110** (10), 1431–1456.

ROY, A. G., BUFFIN-BÉLANGER, T., LAMARRE, H. & KIRKBRIDE, A. D. 2004 Size, shape and dynamics of large-scale turbulent flow structures in a gravel bed river. *J. Fluid Mech.* **500**, 1–27.

SECHET, P. & LE GUENNEC, B. 1999 Bursting phenomenon and incipient motion of solid particles in bed-load transport. *J. Hydraul. Res.* **37** (5), 683–696.

SHIELDS, A. 1936 Anwendung der Ähnlichkeitsmechanik und der Turbulenzforschung auf die Geschiebebewegung. *Mitt. Versuchsanstalt Wasserbau Schiffbau (Berlin)* **26**, 1–26.

SHVIDCHENKO, A. B. & PENDER, G. 2001 Macroturbulent structure of open-channel flow over gravel beds. *Water Resour. Res.* **37** (3), 709–719.

SONG, T. & GRAF, W. H. 1994 Non-uniform open-channel flow over a rough bed. *J. Hydrosci. Hydraul. Engng, Tokyo* **12** (1), 1–25.

STÖSSER, T., RODI, W. & FRÖHLICH, J. 2005 LES of open-channel flow over a layer of spheres. In *Proceedings of the 31st IAHR Congress* (ed. B. H. Jun, S. I. Lee, I. W. Seo & G. W. Choi), CD-Rom. Seoul, Korea, Korea Water Resources Association.

SUMER, B. M. & DEIGAARD, R. 1981 Particle motions near the bottom in turbulent flow in an open channel. Part 2. *J. Fluid Mech.* **109**, 301–337.

SUMER, B. M. & OGUZ, B. 1978 Particle motions near the bottom in turbulent flow in an open channel. *J. Fluid Mech.* **86**, 109–127.

SUTHERLAND, A. J. 1967 Proposed mechanism for sediment entrainment by turbulent flows. *J. Geophys. Res.* **72** (24), 6183–6194.

Thomas, A. S. W. & Bull, M. K. 1983 On the role of wall-pressure fluctuations in deterministic motions in the turbulent boundary layer. *J. Fluid Mech.* **128**, 283–322.

Tomkins, C. D. 2001 The structure of turbulence over smooth and rough walls. PhD thesis, Graduate College, University of Illinois.

Tomkins, C. D. & Adrian, R. J. 2003 Spanwise structure and scale growth in turbulent boundary layers. *J. Fluid Mech.* **490**, 37–74.

Wu, F. C. & Jiang, M. R. 2007 Numerical investigation of the role of turbulent bursting in sediment entrainment. *J. Hydraul. Engng* **133** (3), 329–334.

Zhou, J., Adrian, R. J. & Balachandar, S. 1996 Autogeneration of near-wall vortical structures in channel flow. *Phys. Fluids* **8** (1), 288–290.